Aerosol Atmospheric Rivers:

Climatology, Event Characteristics, and Detection Algorithm Sensitivities

Sudip Chakraborty[1*], Bin Guan[1,2], Duane E. Waliser[1], Arlindo M. da Silva[3]

[1]Jet Propulsion Laboratory, California Institute of Technology, Pasadena, CA, USA

[2]Joint Institute for Regional Earth System Science and Engineering, University of California, Los

Angeles, CA, USA

[3] Global Modeling and Assimilation Office, NASA/Goddard Space Flight Center, Greenbelt,

MD, USA

*Corresponding Author email: sudip.chakraborty@jpl.nasa.gov

Abstract

Leveraging the concept of atmospheric rivers (ARs), a detection technique based on a widely utilized global algorithm to detect ARs (Guan and Waliser, 2019, 2015; Guan et al., 2018) was recently developed to detect aerosol atmospheric rivers (AARs) using the Modern-Era Retrospective analysis for Research and Applications, Version 2 reanalysis (Chakraborty et al., 2021a). The current study further characterizes and quantifies various details of AARs that were not provided in that study, such as AARs' seasonality, event characteristics, vertical profiles of aerosol mass mixing ratio and wind speed, and the fraction of total annual aerosol transport conducted by AARs. Analysis is also performed to quantify the sensitivity of AAR detection to the criteria and thresholds used by the algorithm. AARs occur more frequently over, and typically extend from, regions with higher aerosol emission. For a number of planetary-scale pathways that exhibit large climatological aerosol transport, AARs contribute up to a maximum of 80% to the total annual transport depending on the species of aerosols. Dust (DU) AARs are more frequent in boreal spring, sea salt AARs are often more frequent during the boreal winter (summer) in the Northern (Southern) Hemisphere, carbonaceous (CA) AARs are more frequent during dry seasons and often originate from the global rainforests and industrial areas, and sulfate AARs are present in the Northern Hemisphere during all seasons. For most aerosol types, the mass mixing ratio within AARs is highest near the surface. However, DU and CA AARs over or near the African continent exhibit peaks in their aerosol mixing ratio profiles around 700 hPa. AAR event characteristics are mostly independent of species with mean length, width, and length/width ratio around 4000 km, 600 km, and 7-8, respectively.

1. Introduction

As an important component of atmospheric composition, aerosols have considerable impacts on the convective lifetime and precipitation (Chakraborty et al., 2016; Fan et al., 2016; Stevens and Feingold, 2009; Rosenfeld et al., 2008; Andreae and Rosenfeld, 2008; Rosenfeld et al., 2016, 2014; Seinfeld et al., 2016; Rosenfeld et al., 2013) of convection, the radiation budget via direct and indirect effects (Chylek and Wong, 1995; Kim and Ramanathan, 2008; Huang et al., 2006; Lohmann and Feichter, 2001; Takemura et al., 2005), and the hydrological cycle (Chakraborty et al., 2018; Rosenfeld et al., 2008). In particular, their interactions with cloud microphysics and radiative forcing remain highly uncertain, constituting a large uncertainty in the assessment of climate radiative forcing (IPCC, 2013b, a). Aerosols can also influence a plant's photosynthesis. Aerosols are known to increase the amount of diffuse radiation (Xi and Sokolik, 2012). The implications for plants are that along with decreasing the direct beam photosynthetically active radiation (PAR), the presence of aerosols would lead to greater diffused PAR, which means illumination of a greater portion of plant canopies, including shaded leaves, for which direct PAR was not accessible previously (Niyogi et al., 2004; Knohl and Baldocchi, 2008; Gu et al., 2003). Moreover, aerosols degrade the air quality and visibility, thus pose direct and negative impacts on human health (Gupta and Christopher, 2009; Martin, 2008; Wang and Christopher, 2003; Li et al., 2017a).

With the advent of satellites capable of providing global-scale observations, it has become clear that aerosol loading in the atmosphere is not limited to regions just near their emission sources, but are also transported across continental areas and large expanses of the ocean — emphasizing a source-receptor relationship among these impacts of aerosols. In addition, in-situ measurements have been conducted to detect aerosol transport events over various regions of

70 the world, even in the remote polar regions (Gohm et al., 2009a; Tomasi et al., 2007a; Wang et

71 al., 2011a; Rajeev et al., 2000a; Bertschi et al., 2004a; Qin et al., 2016a; Ackermann et al., 1995;

72 Fast et al., 2014a). Many studies have previously investigated the long-range aerosol transport

73 events between various regions of the world (Prospero, 1999; Sciare et al., 2008; Abdalmogith

74 and Harrison, 2005; Swap et al., 1996; Kindap et al., 2006a; Weinzierl et al., 2017) including

75 inter-continental transport events. Many regions have been studied including the transport events

76 from the Sahara Desert to the United States (Prospero, 1999), Europe to Istanbul (Kindap et al.,

77 2006b), East Asia to California (Fan et al., 2014), and South Africa to the South Atlantic region

78 (Swap et al., 1996). Many other studies have investigated aerosol aging and chemical processes

79 during the transport events (Febo et al., 2010; Kim et al., 2009; Mori et al., 2003; Markowicz et

80 al., 2016; Song and Carmichael, 1999) including the secondary organic aerosol formation and

81 depicted the impact of the long-range aerosol transport on clouds (Wang et al., 2020a; Garrett

82 and Hobbs, 1995), precipitation (Fan et al., 2014), radiation (Ramanathan et al., 2007), and air

83 quality events including the PM2.5 level (Han et al., 2015; Chen et al., 2014; Prospero et al.,

84 2001; Febo et al., 2010). Apart from the studies using satellite and in-situ measurements, climate

85 models have often been used to understand aerosol transport (Takemura et al., 2002; Chen et al.,

86 2014; Ackermann et al., 1995; Fast et al., 2014). As mentioned above, many of these studies

87 used different approaches and methodologies and thus comparing one region to the another

88 around the globe or depicting one species' character of extreme events to another species with a

89 common framework is difficult. Although these studies identify aerosol transport events across

90 the globe, a clear picture about the identification of the extreme aerosol transport events (see

91 methods) using long-term climatological observational data sets, their climatology and major

92   transport pathways, and fractional contribution of those extreme transport events to the global

93   annual transport were lacking.

94   Leveraging the concept of atmospheric rivers (ARs) (Ralph et al., 2020; Zhu and Newell,

95   1994) and a widely used global AR detection algorithm (Guan and Waliser, 2019, 2015; Guan et

96   al., 2018), our previous study developed an aerosol atmospheric rivers (AARs) detection

97   algorithm (Chakraborty et al., 2021a). As with ARs that were studied around the globe using

98   different algorithms in different places, including global change studies, it was hard to get a

99   consistent assessment based on one homogeneous method of identifying the transport events. A

100   value of this study comes from the extension of a well-developed algorithm and applied

101   uniformly around the globe and across species. That study applied the new AAR detection

102   algorithm to five primary aerosol species represented in the MERRA-2 reanalysis – dust (DU),

103   sulfate (SU), sea salt (SS), and organic and black carbon (CA), and showed that aerosols can be

104   transported long distances by AARs, i.e. narrow and elongated channels of very high values of

105   vertically-integrated aerosol transport. It should be noted that aerosol transport and the fractional

106   contribution from AARs is detected over certain regions or the major transport pathways of the

107   globe. For example, except SS aerosols, AARs of other species are not detected over the tropical

108   equatorial regions, especially over the oceans. Moreover, it was found that along major transport

109   pathways, AARs are detected about 20-30 days per year and can be responsible for up to a

110   maximum of 40-80%, depending on the species of aerosols, of the total annual aerosol transport

111   (Fig. 3, Chakraborty et al., 2021a)." That study also illustrated that AAR events can have

112   profound impacts on local air quality conditions.

113   Owing to the relatively large contribution AARs have on the total annual aerosol transport in

114   many regions across the world, and the impacts that AARs can have on regional air quality

115   conditions, it is important to further investigate and quantify the roles AARs play within the

116   climate system and the impacts they have on air quality. For example, our previous study did not

117   characterize and show the vertical profiles of aerosol mass flux and wind of AARs for each

118   aerosol species. However, such information is crucial to improving the understanding of the

119   impacts of aerosols on the global radiative budget since multiple studies have revealed that the

120   aerosols' radiative impact depends on the aerosol composition and their vertical distribution

121   (Keil and Haywood, 2003; McComiskey and Feingold, 2008; Satheesh and Ramanathan, 2000;

122   Mishra et al., 2015). With that motivation in mind, the current study explores the AAR concept

123   further, characterizing and quantifying additional important features of AARs that were not

124   provided in Chakraborty et al. (2021a). These include 1) characteristics of individual AARs such

125   as length, width, length/width ratio, transport strength, and dominant transport direction, 2)

126   seasonal variations, 3) relationship to the spatial distribution of surface emissions, 4) vertical

127   profiles of wind, aerosol mixing ratio, and aerosol mass fluxes, and 5) the major planetary-scale

128   aerosol transport pathways AARs contribute to. As with Chakraborty et al (2021a), we carry out

129   this analysis utilizing the Modern-Era Retrospective analysis for Research and Applications,

130   Version 2 (MERRA-2) reanalysis during 1997-2014, and for all five aerosol species represented:

131   DU, SS, SU, OC, and BC; the latter two are combined into carbonaceous aerosols (CA) in

132   Figures 1 and 2 (Buchard et al., 2017; Gelaro et al., 2017; Randles et al., 2017).

133   **2. Data**

134   For this study, we use the MERRA-2 aerosol reanalysis (Global Modeling and Assimilation

135   Office (GMAO), 2015a) (Global Modeling and Assimilation Office (GMAO), 2015a) that has a

136   horizontal resolution of 0.5° x 0.625° and a temporal resolution of 1 hour (Randles et al., 2017).

137   In particular, most of the analysis is based on the zonal and meridional components of the

138   vertically-integrated aerosol mass flux data. The MERRA-2 aerosol reanalysis data capture the

139   global aerosol optical depth reasonably well and are validated against 793 Aerosol Robotic

140   Network (AERONET) stations' aerosol measurements (Gueymard and Yang, 2020). For

141   example, we have used the variables dust mass flux in the zonal (DUFLUXU) and meridional

142   (DUFLUXV) directions to compute integrated aerosol transport (IAT) values for dust at each

143   grid. MERRA-2 aerosol data have previously been used in studies investigating aerosol

144   microphysical effect and global aerosol transport (Xu et al., 2020; Sitnov et al., 2020;

145   Chakraborty et al., 2021a). Our previous study using MERRA-2 data successfully detected

146   AARs over various regions of the globe, and the AERONET stations located either in the

147   receptor regions or along the path of AARs have shown a substantial increase in the aerosol

148   optical thickness during AAR events (Chakraborty et al., 2021a).

149   To examine the vertical profiles of aerosol amount, wind and aerosol mass fluxes (i.e. Figure

150   4), we use MERRA-2 3-hourly, instantaneous, aerosol mixing ratio data (inst3_3d_aer_Nv, last

151   accessed : June 2021) that provide aerosol mass mixing ratio at 72 vertical levels. To assess the

152   information about the zonal and meridional wind, we use MERRA-2's associated meteorological

153   fields (inst3_3d_asm_Nv, last accessed : June 2021) with the same resolution as the aerosol mass

154   mixing ratio data (Randles et al., 2017). In addition, we also use MERRA-2 time-averaged,

155   single-level, assimilated aerosol diagnostics (Global Modeling and Assimilation Office

156   (GMAO), 2015b) datasets (MERRA-2 tavgU_2d_adg_Nx) to describe the spatial distribution of

157   the emissions of aerosol particles at the surface to examine the relationship between source

158   regions and frequency of occurrence of AARs. MERRA-2 accounts various sources for

159   emissions (Randles et al., 2017). Dust emissions in MERRA-2 use a map of potential dust source

160   locations. Emissions of both DU and SS are wind driven for each size bin and parameterized. Sea

161 salt emission is estimated using the sea surface temperature and the wind speed dependency

162 with sea salt emission parameterization depends on the friction velocity. For SS, lake emissions

163 are also considered. SU aerosol emissions derive from both natural and anthropogenic

164 sources. Inventories for sulfate includes volcanic sulfur dioxide (SO_2) emissions as well as those

165 from the aircraft, energy-sectors, and anthropogenic aerosol sources. Emissions of CA and SU

166 aerosols in MERRA-2 come from various inventories over the time. From 2010, the Quick Fire

167 Emissions Dataset version 2.4-r6 is used. Locations of fires are obtained from MODIS level-2

168 fire and geolocation products. Please see table 1 of Randles et al., 2017 for details. Before that

169 MERRA-2 utilizes the Global Fire Emission Dataset from MODIS. MERRA-2 also applies

170 biome-dependent correction factors, fractional contributions of emissions from different forests

171 with applying correction to the monthly mean emissions that cover 1980–96 and are based on

172 Advanced Very High Resolution Radiometer, the Along Track Scanning Radiometer, and the

173 Total Ozone Mapping Spectrometer Aerosol Index.

174

175 **3. Methodology**

176 The AR detection algorithm designed by (Guan and Waliser, 2015)) was to detect and study

177 ARs based on a combination of criteria related to the intensity, direction, and geometry of

178 vertically integrated water vapor transport (IVT). The algorithm and associated AR detection

179 databases (based on multiple reanalysis products) have been widely used by the AR research

180 community (Chapman et al., 2019; Dhana Laskhmi and Satyanarayana, 2020; Edwards et al.,

181 2020; Gibson et al., 2020; Guan et al., 2020; Guan and Waliser, 2019; Huning et al., 2019;

182 Jennrich et al., 2020; Nash and Carvalho, 2019; Sharma and Déry, 2020; Wang et al., 2020;

183   Zhou and Kim, 2019). Details about the AAR algorithm and the modifications made to the AR

184   algorithm to make it applicable for AARs are provided below.

185   In the initial AAR algorithm (Chakraborty et al., 2021a), we detect AARs daily at four-time

186   steps (00, 06, 12, and 18 hours UTC) for a period of 18 years during 1997-2014 and separately

187   for each aerosol species. To compute total IAT over each grid cell at each time step for any

188   species (n) of aerosols we calculate $IAT_n = \sqrt[2]{IATU_n^2 + IATV_n^2}$ where IATU and IATV denote

189   the vertically integrated aerosol mass flux in the zonal and meridional directions, respectively.

190   We are interested in identifying extreme transport events; thus, we first compute the 85th

191   percentile of the IAT magnitude over each grid cell during 1997-2014. Grid cells with IAT

192   magnitude less than the 85th percentile threshold are discarded. The remaining grid cells serve as

193   input to the following five steps to 1) isolate objects (i.e., contiguous areas) of enhanced IAT

194   with values above the 85th percentile; 2) check the consistency of the IAT directions at each grid

195   cell within an IAT object, to retain only those objects where at least 50% of the grid cells have

196   IAT directions within 45° of the direction of the mean IAT of the entire object; 3) retain the

197   stronger 50% of those objects detected in the previous step based on the object-mean IAT; 4)

198   retain objectives only if the direction of object-mean IAT is within 45° of the along-river axis to

199   ensure that the direction of the aerosol transport is aligned with the river; 5) apply length and

200   length-to-width ratio criteria and retain only those objects longer than 2000 km an aspect ratio

201   greater than 2. At the end of these steps, the objects that remain are referred to as AARs and are

202   further characterized in this study. We also show the sensitivity of the detection of AARs to key

203   threshold values used in the above steps in Figure 9.

204   In developing the AAR detection algorithm (Chakraborty et al., 2021a), only three changes

205   were made to the original AR detection algorithm. In step 1 of the AR moisture algorithm, a

206   fixed lower limit of IVT, specifically 100 kg m^{-1} s^{-1}, is applied globally to facilitate detection of

207   ARs in polar regions where IVT is extremely weak climatologically due to the very cold, dry

208   atmosphere. We found that this additional filter is not needed for AAR detection. In addition,

209   given the strong meridional moisture gradient between the tropics and extratropics, ARs are

210   primarily recognized as the dominant means to transport water vapor poleward (Zhu and Newell,

211   1998). Accordingly, the AR algorithm is designed to detect IVT objects with notable transport in

212   the poleward direction. However, since there is no similar and dominant planetary gradient in

213   aerosol concentration in the north-south direction, we removed this constraint on meridional IAT

214   for AARs and instead applied a constraint on the total IAT (i.e., zonal and meridional

215   components combined). Finally, Chakraborty et al. (2021a) computed the climatological 85th

216   percentile threshold IAT values for each month based on the 5 months centered on that month, as

217   in the original AR algorithm (Guan and Waliser, 2015). However, it was found that a 3-month

218   window better resolves the annual cycle of IAT and meanwhile still retains sufficient sampling

219   over the period of 1997–2014. For example, the IAT 85th percentile for February is calculated

220   using the IAT values four times each day during January-March of 1997-2014.

221   AAR frequency at each grid cell is calculated as percent of time steps AARs are detected at

222   that grid cell, and expressed in units of days/year for annual means (by multiplying the

223   percentage by 365 days/year) and days/season for seasonal means (by multiplying the percentage

224   by 91 days/season). The mean zonal and meridional IAT associated with AARs over each grid

225   cell at latitude φ and longitude λ are calculated as:

226   Mean IATU$(\varphi, \lambda) = \sum_{1}^{N}$ IATU $(\varphi, \lambda)/N$ and Mean IATV$(\varphi, \lambda) = \sum_{1}^{N}$ IATV $(\varphi, \lambda)/N$

227   where N is the number of times AARs were detected over that grid cell.

228   To obtain the fraction of total (i.e., regardless of AAR or non-AAR) annual transport

229   conducted by AARs of five different aerosol species, we first temporally integrate IATU and

230   IATV over all the time steps when AARs were detected over a grid cell at latitude φ and

231   longitude λ as

$$\text{Total IATU}(\varphi, \lambda) = \int_0^T \text{IATU}(\varphi, \lambda, t)\, dt \quad (1a)$$

$$\text{Total IATV}(\varphi, \lambda) = \int_0^T \text{IATV}(\varphi, \lambda, t)\, dt \quad (1b)$$

235   where dt is the duration between each time step (6 hours), and T is the total duration for 18 years.

236   Based on that, the magnitude of annual AAR IAT, which is a scalar quantity, at each grid cell is

237   calculated as $\text{Total\_AAR\_annual\_IAT}_{\varphi,\lambda} = \sqrt[2]{\text{Total IATU}(\varphi, \lambda)^2 + \text{Total IATV}(\varphi, \lambda)^2}/18$.

238   Similarly, we compute $\text{Total\_all\_annual\_IAT}_{\varphi,\lambda}$ for all the time steps (i.e., AAR and non-AAR

239   combined). Next, since the annual AAR IAT and annual total IAT are not expected to be in the

240   same exact direction, we project the former onto the latter. For that, the directions of the two

241   vectors are obtained as

$$\text{ß}_{All} = \tan^{-1}(\text{Total IATU}(\varphi, \lambda)/\text{Total IATV}(\varphi, \lambda)) \text{ for all events} \quad (2a).$$

$$\text{ß}_{AAR} = \tan^{-1}(\text{Total IATU}(\varphi, \lambda)/\text{Total IATV}(\varphi, \lambda)) \text{ for AAR events} \quad (2b).$$

244   Finally, the fraction of total annual transport conducted by AARs is obtained as $\text{Frac}_\varphi = $

245    $\text{Total\_AAR\_annual\_IAT}_{\varphi,\lambda} \times \cos(\text{ß})/\text{Total\_all\_annual\_IAT}_{\varphi,\lambda}$, where $\text{ß} = \text{ß}_{All} - \text{ß}_{AAR}$.

246   **4. Results**

247   **4.1 Overall aerosol transport and surface emission**

248   To provide a background for characterizing the seasonality of AARs, we first illustrate the

249   seasonal variability of the overall aerosol transport (i.e., regardless of AAR conditions) during

250   1997-2014 (Fig. 1). Here, we combine black carbon (BC) and organic carbon (OC) aerosols,
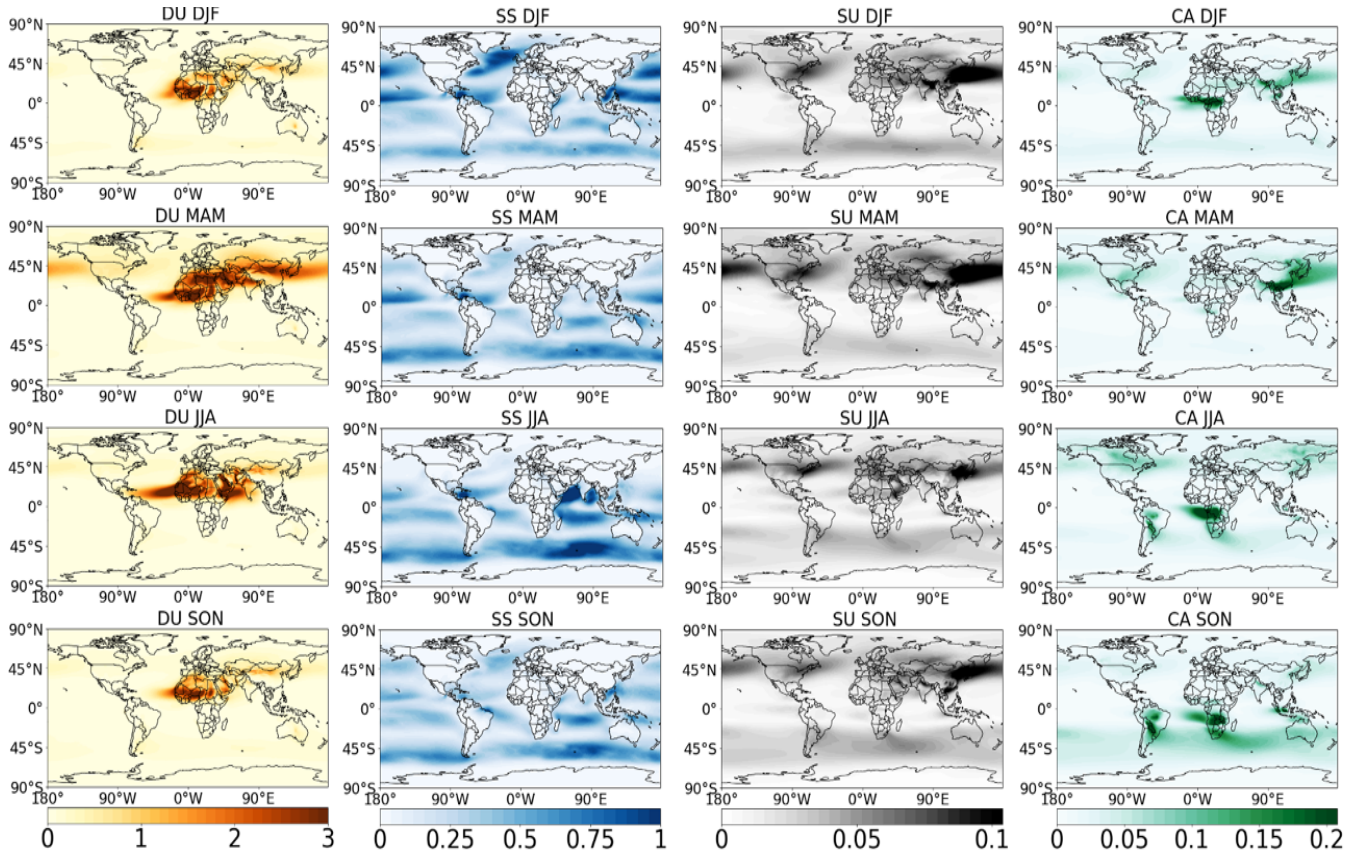
Figure 1. MERRA-2 vertically integrated aerosol transport (IAT, 10^{-3} kg m^{-1} s^{-1}) in 4 seasons (DJF: December-February; MAM: March-May; JJA: June-August, and SON: September-November) during 1997-2014.

251   denoted as CA, owing to their similar sources and seasonality (BC and OC are accounted for

252   separately in subsequent analysis of AARs). Dust IAT (first column, Fig. 1) is higher during the

253   MAM and JJA seasons. Global deserts, such as the Sahara Desert, Gobi Desert, and Taklamakan

254   Desert and the Middle East act as a significant source of dust aerosols year-round (Fig. 2A)

255   emitting more than 2 x 10^{-9} kg m^{-2} s^{-1} of dust, primarily in the northern Spring. The sea-salt IAT

256   (second column, Fig.1) increases during the winter seasons of the Northern and Southern

257   Hemispheres due to the increased mean westerly flow and storm activities during these seasons.

258   Annual maps of SS emission (Fig. 2B) show that a large number of SS aerosols are emitted over

259   the global oceans, especially over the tropical oceans because of the convective activities and in

260   the midlatitudes where synoptic storm activities are dominant. Sulfate IAT (SU, third column,

261   Fig. 1) is high over a region between China and the North Pacific Ocean region, extending up to

262   the western US, during all seasons with the lowest SU IAT values in JJA. The large SU IAT

263   values (Figure 2C) are likely due to high emissions of SO_2 over China (Dai et al., 2019; Wang et

264   al., 2013) coupled with strongly varying synoptic flows. A secondary region of higher amount of

265   SU IAT is also detected between the eastern US and the northwestern Atlantic Ocean as a high

266   amount of SO_2 is emitted east of the Rocky Mountains, particularly over the Ohio valley (Fig.
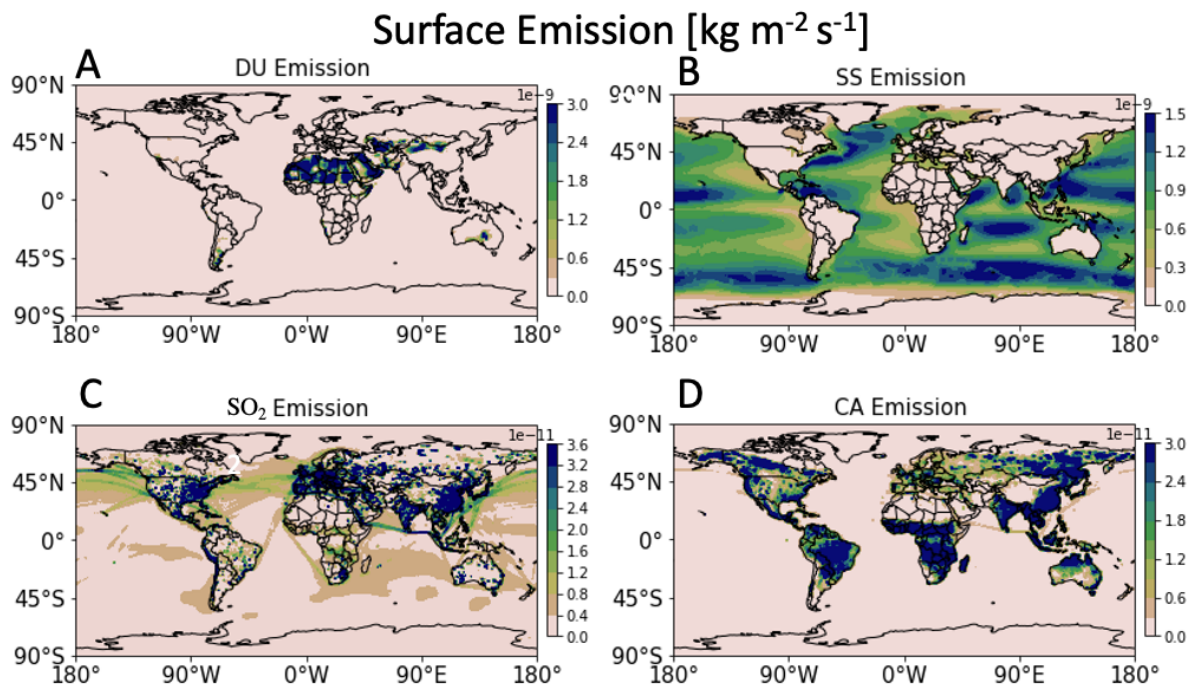
Figure 2. Annual surface emission (kg m^{-2} s^{-1}) of (A) DU, (B) SS, (C) SO_2 and (D) CA (BC+OC)
aerosol species during 1997-2014 from the MERRA-2 data.

267   2C). Figure 2C also shows some SO_2 is emitted due to global shipping activities.

268   Globally, boreal and rainforests are the most significant contributors to the CA aerosols (Fig.

269   2D). Accordingly, it appears that the Congo rainforest dominates the Amazon rainforest in terms

270   of CA IAT (right column, Fig. 1). The Amazon rainforest region has higher IAT during its dry

271   and transition seasons, and lower IAT in the wet season. Similarly, the Congo rainforest releases

272 a high amount of CA aerosols during the dry season (JJA) and another peak in the Sahel during

273 DJF (Fig. 2D). An increase in dry period CA IAT might be due to the increased vegetative stress,

274 forest fire, and agricultural burning over these two regions. However, it is interesting to note that

275 the Congo rainforest also emits CA aerosols during the boreal autumn (SON) rainy season,

276 which is the stronger of the two rainfall seasons in this region, but not during the MAM rainy

277 season. In MAM, the tropical rainforests over eastern India, Myanmar, and southern China have

278 higher CA IAT values. Emissions from the boreal forests appear to be less than that of the

279 rainforests. Over most of the midlatitudes in the Northern Hemisphere, the emissions of CA

280 aerosols (Fig. 2D) (also IAT values, Fig. 1D) is less than that over the global rainforests and

281 China in all four seasons (Fig. 1). As a result, although CA (OC and BC) AARs are more

282 frequent over the midlatitude region, the mean IAT by those rivers are less than those AARs that

283 originate from the global rainforests and China (Chakraborty et al., 2021a). These results point

284 out the existence of seasonality and variability in the overall aerosol emission and transport. As a

285 result, we expect the frequency and intensity of AARs might also vary among different seasons

286 in accordance with the distribution of surface emissions.

287 **4.2 AAR frequency and intensity**

288 To illustrate characteristics of individual AAR objects, Fig. 3 shows examples of AARs of

289 each species, including the location, shape, and transport direction and magnitude. Also indicated

290 in the figure is the length and width of each illustrated AAR. Figure 3A shows all the DU AARs

291 detected on 25th June, 2008 at 1200 UTC. Many of those DU AARs are detected between the

292 Sahara Desert and the Caribbean, the middle east region and Europe, over the central US, and

293 over the Patagonia region. Figure 3D shows details of one DU AAR (encircled in Fig. 3A) that

294 extends from the western boundary of the Sahara Desert to the southern US and Caribbean and
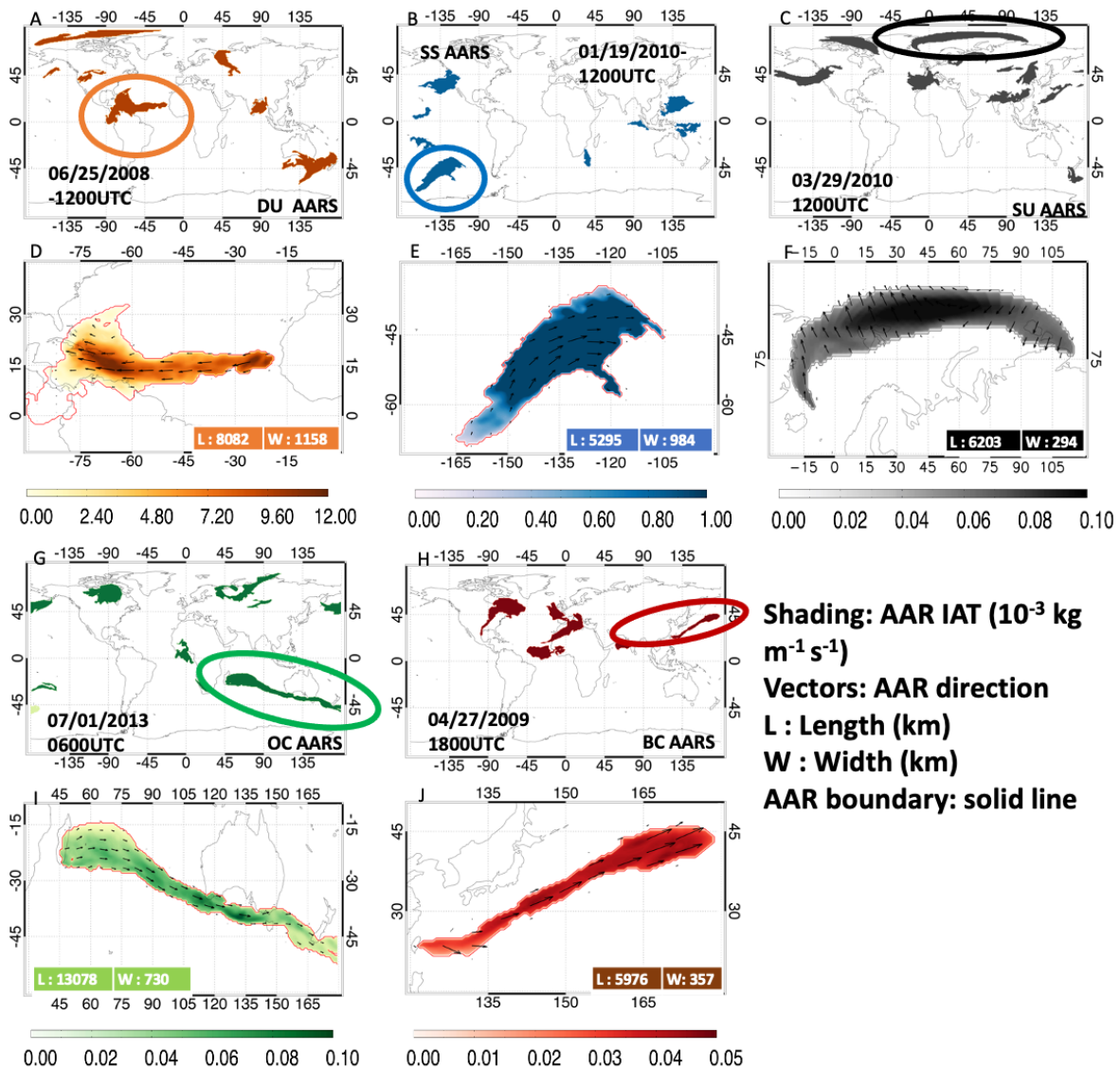
Figure 3: Detection of five different species of aerosols atmospheric rivers. Each panel in the 1st and 3rd rows show all AARs detected for a given species at an arbitrary time step; see bottom of each panel for the aerosol species and time stamp. Each panel in the 2nd and 4th rows shows detail (see legend) of a specific AAR from the corresponding panel above.

295   has IAT values greater than 12 x 10^{-3} kg m^{-1} s^{-1}. The AAR is 8082 km long and 1158 km wide.

296   Similarly, we show details of one SS AAR (Fig. 3E) with a length of 5295 km and a width of

297   984 km (IAT ~ 1.0 x 10^{-3} kg m^{-1} s^{-1}) over the Southern Ocean among other AARs detected on 19th

298   January 2010 at 1200 UTC (Fig. 2B). Unlike DU AARs, SS AARs are located mostly over the

299   ocean (see also Fig. 4) and carry the extratropical AR signature. SS AARs over the tropical

300   regions appear to be smaller than the extratropical AARs in Figure 3B.

301   A number of SU AARs occurred in the polar region due to the Eyjafjallajökull volcanic

302   eruption (Fig. 3C). The volcano, located in Iceland, erupted on the 20th March 2010, causing

303   disruption to the aviation industry

304   (https://volcanoes.usgs.gov/volcanic_ash/ash_clouds_air_routes_eyjafjallajokull.html). In Figure

305   3F, we show details of one of these SU AARs on the 29th March 2010. The SU AAR is 6203 km

306   long and 294 km wide and transported a large amount of SU aerosols (IAT $\sim$ 0.1 x 10^{-3} kg m^{-1} s^{-1})

307   into and across the polar region. It is important to notice that MERRA-2 did not include the ash

308   aerosols that were co-emitted with the SO_2 plumes that were eventually converted into sulfate

309   aerosols by gaseous and aqueous processes. In April 2010, out algorithm detected ~80 SU AARs

310   (at every six hours of interval i.e., 20 SU AAR days) originating over that region and

311   propagating to different directions.

312   Herein forth, we separately show the CA rivers as OC and BC rivers, especially because BC

313   AARs can significantly impact the radiative forcing compared to OC AARs and because the

314   mean mass of aerosols being transported by the OC is about five times that of BC AARs (Fig. 4).

315   Figure 3G shows examples of OC AARs detected on the 1st July 2013. We show details of one

316   OC AAR that stretches from Madagascar to New Zealand in Figure 3I. The OC AAR is 13078

317   km long and 730 km wide and flows west over the Indian Ocean with IAT of ~0.1 x 10^{-3} kg m^{-1} s^{-}

318   ^{1}. Figure 3H shows a few BC AARs detected on 27th April 2009. BC AARs often originate near

319   the China-northwestern Pacific Ocean region (see also Fig. 4). We show the details of one such

320   BC AAR in Figure 3J. It is to be noted that the IAT values of BC AARs are smaller than the OC

321 AARs; however, they might play a significant role in the atmospheric radiation budget owing to

322 the capability of BC aerosols to absorb solar energy.
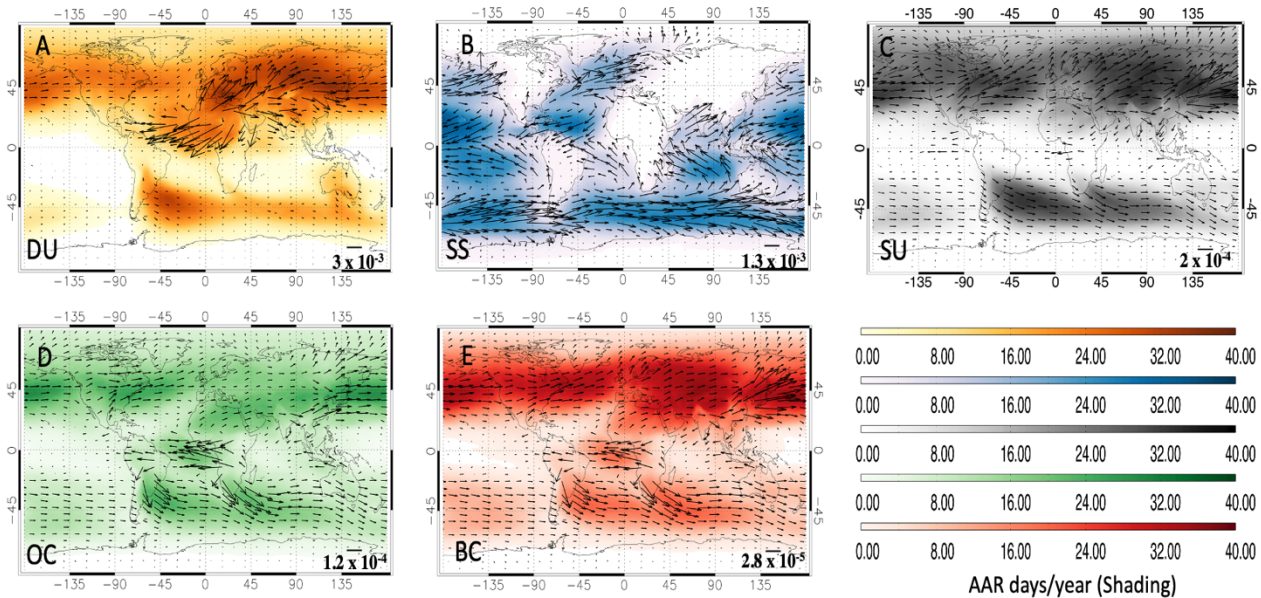
Figure 4. Annual climatological AAR frequency (days/year; shading) and IAT (arrows; kg m^{-1} s^{-1}) during 1997-2014 based on MERRA-2. (A) Dust; (B) Sea salt; (C) Sulfate; (D) Organic carbon; (E) Black carbon. Scales for the IAT vectors are provided in the lower right side of each plot.

323   To illustrate the overall climatology of AARs, Figure 4 shows the annual mean frequency of

324 occurrence (shading; days per year) and the mean IAT (arrows; kg m^{-1} s^{-1}) associated with AARs.

325 Figure 4A shows that a strong anticyclonic motion over the Sahara Desert is associated with

326 many DU AARs, consistent with the annual DU emission (Fig. 2A) and seasonal DU IAT (Fig. 1

327 – leftmost column) over that region. Around 30 AAR days/year (shades) carry on average 3-15 x

328 10^{-3} k gm^{-1} s^{-1} (vectors) of dust from the Sahara Desert over the North Atlantic Ocean and reach

329 the southern US and the Caribbean regions. A similar number of AARs also transport aerosols

330 towards Europe and the middle east region. A relatively high number of DU AARs are detected

331 over China, Mongolia, and Kazakhstan; however, the mean transport over these regions by

332   AARs is lower (IAT ~1 x 10^{-3} kg m^{-1} s^{-1}) than those originating from the Sahara Desert. The

333   Southern Hemispheric deserts also emit numerous AARs but with a smaller amount of dust

334   transport as the dust emission (Fig. 2A) and IAT (Fig. 1) are low over there. Overall, the Sahara

335   Desert dominates any other deserts in the world regarding the formation of the strongest and

336   most intense DU AARs.

337   Figure 4B shows the climatological maps of SS AARs. SS AARs are mostly located over the

338   global oceans, especially over the tropical and subtropical trade wind regions. The SS AARs in

339   the midlatitudes carry the signature of the storm tracks, and have distributions similar to ARs

340   (Guan and Waliser, 2015). Every year, in the midlatitude region, 30-40 ARs are detected

341   (Chakraborty et al, 2021a), whereas ~20 AAR days/year occur in the mid-latitudes with mean

342   IAT of ~2 x 10^{-3} kg m^{-1} s^{-1}. The distributions between ARs and SS AARs are not quite the same;

343   the SS AARs are biased equatorward toward the trade winds. In comparison, tropical SS AARs

344   are more frequent but have less IAT than the midlatitude SS AARs. Around 30 SS AARs have

345   mean IAT of ~1 x 10^{-3} kg m^{-1} s^{-1} over the tropical region.

346   It is important to note SU AARs are more frequent (~40 days/year, Fig. 4C) in the Northern

347   Hemisphere than in the Southern Hemisphere, consistent with the predominance of emissions of

348   SO_2 over China, Europe, and the eastern US (Fig. 2C) owing to anthropogenic emissions as well

349   as biogenic activities in these regions. It is important to note that MERRA-2 aerosols data don't

350   account for biogenic sources like Carbonyl Sulfide in the version of the data we have used for

351   this study. The SU AAR hotspot regions over the Southern Hemisphere include pathways from

352   the southern edges of the global rainforests to the South Indian, South Atlantic, and Southern

353   Oceans. Mean IAT (~0.2 x 10^{-3} kg m^{-1} s^{-1}) by SU AARs is lower than that of the DU and SS

354   AARs. Many BC and OC AARs originate from the global rainforests, such as the Congo and

355 Amazon, and from the regions that are susceptible to biomass burning and CA aerosol emissions,

356 such as Europe, the eastern US, industrialized areas over eastern China, and north India.

357 Annually, 20-40 BC or OC AARs are generated from these regions. It appears that BC AARs are

358 more numerous than the OC AARs; however, OC AARs have larger IAT than BC AARs.

359 **4.3 Vertical profiles of AAR aerosol mass flux and wind**

360   To understand the anomalous atmospheric conditions that account for an AAR event, it is

361 important to know the relative contribution of the two quantities that make up these IAT

362 extremes, namely the aerosol mixing ratio and the wind speed. Also, as mentioned before, the

363 altitude of aerosol particles within AARs can be of importance due to aerosol impacts on the

364 radiation budget, convective anvil lifetime (Bister and Kulmala, 2011), cloud formation (Froyd

365 et al., 2009; Khain et al., 2008), and air quality near the surface. Here, we characterize the

366 vertical profiles of the AARs at a number of different locations with high AAR frequency (see

367 the inset map in the middle column; based on Fig. 4). For example, the orange box over the

368 Sahara-Caribbean pathway experiences a presence of 25-30 AARs per year (Fig. 4A). Based on

369 our analysis between 1997-2014, the profiles shown in Figs. 5A, 5B, and 5C shows the mean and

370 standard deviation of ~400-500 AARs.

371   It is important to keep in mind that the aerosol vertical structure in MERRA-2 is not directly

372 constrained by measurements, and are chiefly determined by the injection height of the emissions

373 as well as turbulent and convective transport processes parameterized in the model. Evaluation of

374 the vertical structure of MERRA-2 aerosols appears in Buchard et al. (2017). Buchard et al.

375 (2017) has attempted to use Cloud-Aerosol Lidar and Infrared Pathfinder Satellite Observation

376 (CALIPSO) to examine the vertical structure of aerosols in MERRA-2. The left column of Fig. 5

377 shows composite vertical profiles of aerosol mass fluxes for each aerosol species; both those for
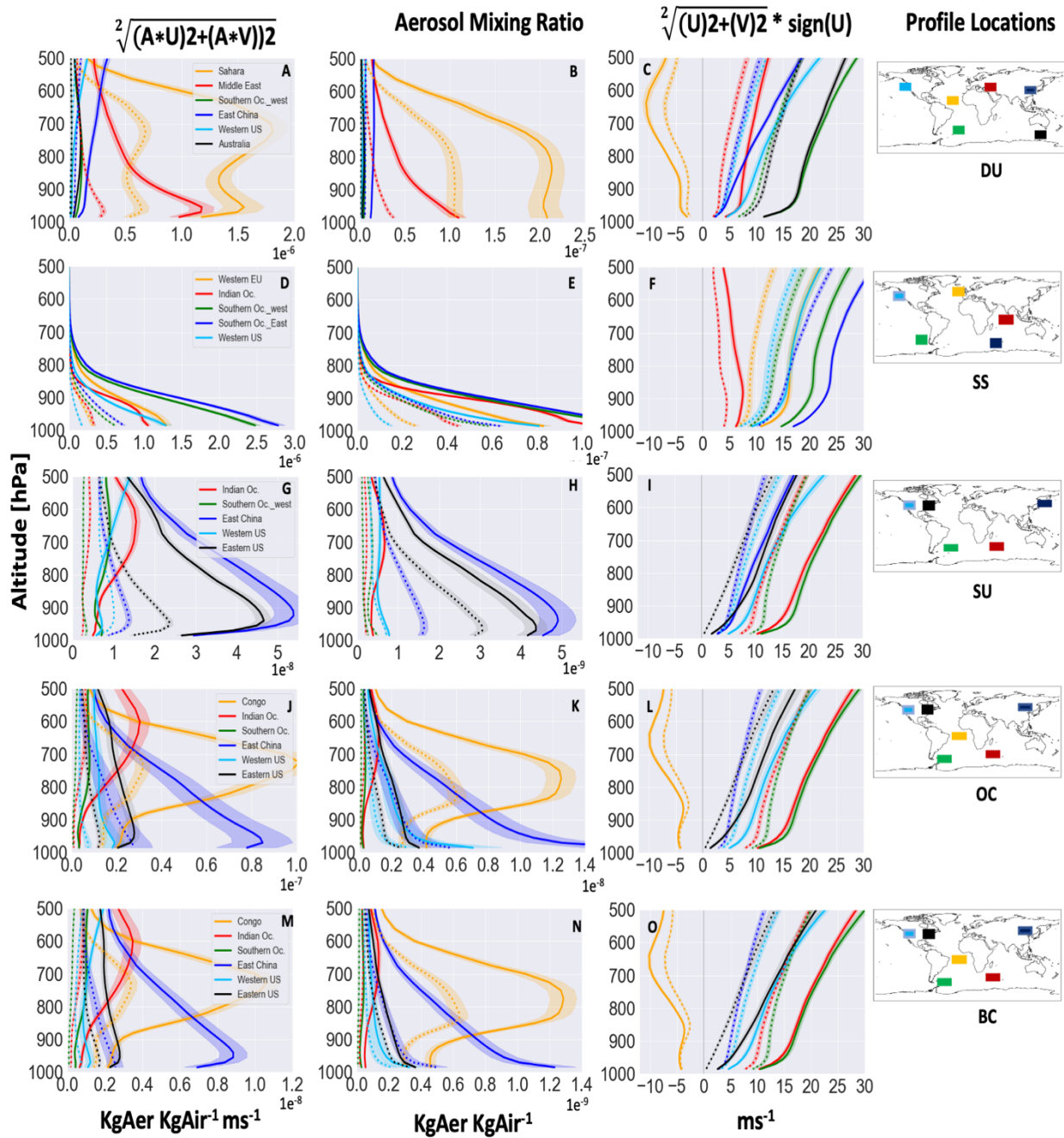
Figure 5. Average vertical profiles of (left) aerosol mass fluxes, (center) aerosols mixing ratio, and (right) wind speed over a number of locations for AAR events (solid) and All (dotted) time steps. Please see the AAR frequency maps in the inset of the middle panel for the locations chosen to calculate the profiles. In the right column, a sign convention (see column title) is used to highlight the general east-west direction of the wind speed profiles.

378   AARs (solid) and for all time steps regardless of AAR conditions (dotted) are shown for

379   comparison. Mean fluxes of the synoptic AAR events is larger than the overall annual mean over

380   all the regions, not unexpected since AARs represent the extreme transport events. For DU

381   AARs (Fig. 5A), the strongest transport is observed between the Sahara Desert and North

382   Atlantic/Caribbean (orange) as well as western Europe/middle-east (red) pathways. Flux values

383   decreases with altitude within AARs that transport aerosols from the Sahara Desert to the

384   Europe/Middle East region (red). However, AARs that transport aerosols from the Sahara Desert

385   to the North Atlantic region (orange) have peak IAT values near 750 hPa. There is also a

386   secondary peak at the 960 hPa (Fig. 5A). The aerosol mixing ratio (Fig. 5B) slightly decreases

387   from the surface up to a height of 960 hPa and then increases above it. This might suggest the

388   influence of the gravitational force and settlement on the aerosol mixing ratio as observed in

389   many of the aerosol mixing ratio profiles of other species over other regions (for example, the

390   red line showing the aerosol mixing ratio profile for the Sahara to European pathway). However,

391   a smaller peak in the wind profile (Fig. 5C) around 950 hPa indicates the influences from the

392   low-level jets and the seasonal variations of trans-Atlantic dust transport that have not been

393   studied yet. A detailed seasonal analysis is required to understand the existence of the smaller

394   peak at 960 hPa. However, the presence of the African easterly jet-north or AEJ-N above,

395   centering 600-700 hPa, further lifts the aerosols and attain a peak around 750 hPa.

396   We also show the vertical aerosol mixing ratio profiles (middle column) and the wind

397   profiles (right column) separately to help disentangle their influences on the aerosol flux profiles.

398   Given the very few globally gridded datasets to use for this purpose, we have relied on the data

399   provided in the MERRA2 data, which in this case is provided as aerosol mixing ratio. Figure 5B

400   shows that high aerosol levels inside AARs over the Sahara Desert to Caribbean pathway extend

401   vertically up to the 700 hPa with a peak around 750 hPa, unlike any other regions analyzed. The

402   third column, which shows the mean wind speed profile $\sqrt[2]{U^2+V^2}$ multiplied by the sign of the

403   zonal wind to show the east-west direction of the AARs, confirms the influence from the AEJ-N

404   (Cook, 1999; Wu et al., 2009) on AARs' wind profile that peaks around 650 hPa and lifts

405   aerosols over this region (Fig. 4C). Higher flux values near the surface are due to a high aerosol

406   mixing ratio, but as altitude increases higher flux values inside AARs is contributed by both the

407   aerosol lifting and the high zonal wind speed of AEJ-N between the Sahara Desert and the North

408   Atlantic Ocean region. Other regions like the Southern Ocean (near South America), Australia,

409   eastern China, and western US have less aerosol mixing ratio as compared to the Sahara to the

410   North Atlantic Ocean/Caribbean and Sahara to Europe/Middle east pathways. Wind speed

411   contributes to larger flux values as altitude increases over some of these locations near eastern

412   China, the Southern Ocean, Australia, and the western US, however, their flux values are less

413   than those taking off the Sahara Desert.

414   Aerosol flux and mass mixing ratio profiles for SS species (Figs. 5D and 5E) decreases with

415   altitude. This is because the SS particles are typically found within the boundary layer (Gross

416   and Baklanov, 2007) and are larger in size, and often form due to high wind speed and surface

417   evaporation along the storm tracks and may not travel long distances outside the storm tracks

418   (Sofiev et al., 2011; May et al., 2016). The largest aerosol mixing ratio and IAT values are

419   observed over the Southern Ocean consistent with the persistent and year-round AAR activities

420   over there.

421   Consistent with the SO_2 emission (Fig. 2C), eastern China (blue line) dominates in terms of

422   SU aerosol mass mixing ratio by a factor of 5 as compared to the other regions (Fig. 5H)

423   analyzed and shown here. The aerosol mixing ratio (Fig. 5H) and the flux values (Fig. 5G)

424   increase with height, attain a peak around 900 hPa over there, probably exhibiting the impact of

425   the boundary layer inversion effect on the accumulation of the pollutants (Li et al., 2017b).

426   Above 900 hPa, both the aerosols mass mixing ratio and flux values gradually decrease.

427   However, SU aerosol mass mixing ratio decrease when those AARs reach the western US by 5

428   times (Figs. 5H). Owing to the fact that the eastern US originates many SU AARs than can

429   contribute to a transatlantic transport driven by strong westerly winds, we have also computed

430   the IAT profiles of SU AARs generated over there. Figures 5G and 5H show that AARs over the

431   eastern US Also have a high IAT (Fig. 5G) and aerosol mass mixing ratio (Fig. 5H). Flux

432   profiles and aerosols mixing ratio over the Indian Ocean (red) and Southern Ocean (green) show

433   different behavior. Aerosols appear to be continental in origin and are lifted to attain a peak

434   concentration around 650 hPa. Contribution from wind speed (Fig. 5I) as compared to aerosol

435   mixing ratio (Fig. 5H) appears to be less on the SU flux profiles (Fig. 5G) since the wind speed

436   associated with AARs is the highest over the Indian and Southern Ocean, but the largest flux

437   values are associated with the AARs over the eastern China region which have the largest

438   aerosol mass mixing ratio.

439   Next, we examine the vertical profiles of CA AARs over the Congo basin, the western US,

440   the eastern China, the Indian Ocean, and the Southern Ocean. As in the case of dust aerosols over

441   the Sahara Desert to North Atlantic transport pathway (Fig. 5A, orange line), both the OC and

442   BC AARs off the Congo basin show elevated flux values around 700 hPa (Figs. 5J and 5M). It is

443   to be noted that the wind speed within AARs peaks around 650 hPa – suggesting the influence

444   from the AEJ-South (Adebiyi and Zuidema, 2016; Chakraborty et al., 2021b; Das et al., 2017) on

445   the AARs' wind profile (Figs. 7K and 7N) that might be responsible for the peaks in the aerosol

446   mixing ratio profiles around 750 hPa (Figs. 5L and 5O) instead of the exponential profiles as

447   observed in most of other regions. AARs over eastern China (blue) also carry a large amount of

448   near-surface aerosol particles that contribute to large BC and OC IAT values in this region.

449   However, when those AARs reach the western US, the amount of BC and OC aerosol mass

450   mixing ratio significantly decreases by $\sim$ 8 times, presumably because of the settlement and

451   removal of the aerosol particles during the transport. As compared to SU AARs, the IAT values

452   and aerosol mass mixing ration of OC and BC AARs over the eastern US is significantly lower

453   (3-4 times less) than those originating from China and the Congo rainforest. Wind speed appears

454   to have less influence on the flux profiles since the Indian Ocean and the Southern Ocean has the

455   largest (smallest) wind speed (flux values) associated with the AARs.

456   **4.4 Fraction of total annual transport accounted for by AARs**

457   It is apparent from Figure 5 that the mean IAT averaged over AAR time steps is greater than

458   the mean IAT averaged from all time steps. This is not surprising since AARs detected by our

459   algorithm represent the extreme transport events (see Section 2 for definition and methodology).

460   Considering that the original analysis on water vapor ARs (Zhu and Newell, 1998) highlighted

461   that 90% of the poleward transport of water vapor in the midlatitudes occurred in a relativley

462   small number of extreme transport events (i.e. ARs), a similar question can be raised here for

463   AARs. Specifically, what fraction of the total annual aerosol transport is acounted for by the 20-

464   40 AAR days that occur each year on average (Fig. 4)? Also, do AARs transport a higher

465   fraction of the total global annual transport over the major aerosol transport pathways, and is this

466   dependent on aerosol species? In Figure 6, we show the fraction of total annual IAT accounted

467   for by AARs (shades), counting only the component of AAR transport in the direction of the

468   total annual transport (arrows). Figure 6A shows that annually, $\sim$ 40000-100000 kg m^{-1} of DU

469   IAT is transported by All events (i.e. considering all data points in the record) that originate from

470   the Sahara Desert. Near the equator, the fractional transport by AARs (F_{AAR}) is around $\sim$20%
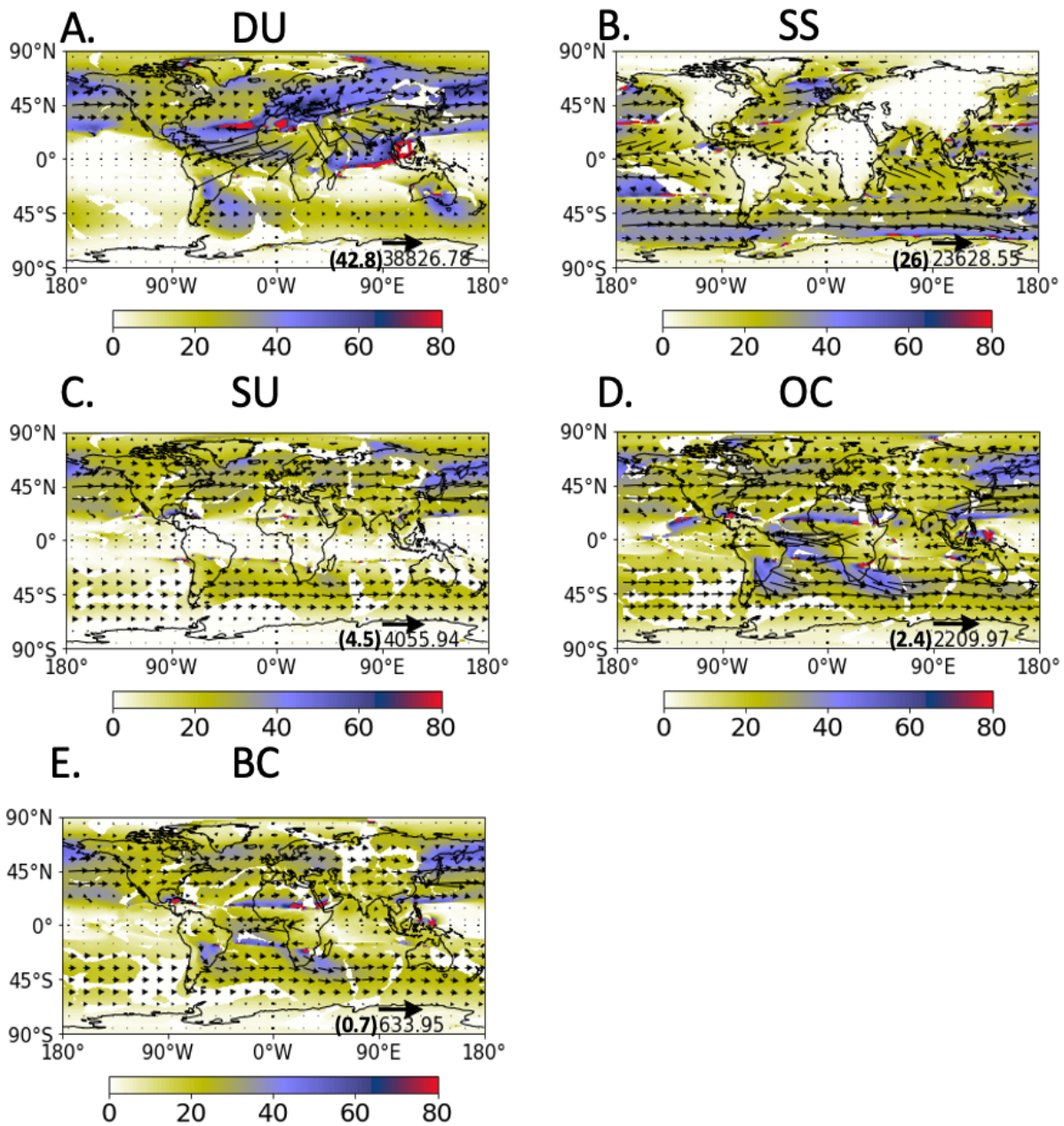
Figure 6. Fraction of annual total IAT transport (arrows; (tons) kg m^{-1}) accounted for by AARs (%; shading) of five different aerosol species.

471 over the Atlantic Ocean in the direction of the Amazon rainforest (Fig. 6A), which is realized

472 within ~30 AAR days per year (see Fig. 4A). In this same longitude sector, F_{AAR} gradually

473 increases with latitude and reaches up to 80% around 35°-40° N where AARs act to transport

474   dust from the Sahara Desert to Europe and the middle-east region. Over Mongolia and China, the

475   total annual IAT is ~20000-40000 kg m^{-1} and about 30-40 AAR days per year (Fig. 4A)

476   contribute up to ~40-50% of that transport. In the Southern Hemisphere, Patagonia and South

477   American drylands give rise to ~4000 kg m^{-1} of annual dust transport and AARs contribute to a

478   maximum of 20-40% of that transport in about 20-30 AAR events per year (Fig. 4A). Over some

479   regions far from the dust source region, such as over the maritime continent, the annual IAT

480   value is very less by All events (Fig. 6A). About 5 AARs (shading, Fig. 4A) with very small

481   object-mean IAT values (arrows, Fig. 4A) are observed over there each year. It appears that

482   although AARs are not frequent (~ 5 AARs/year) over there, they are responsible for 80-100% of

483   the total annual transport.

484   SS AARs are far more frequent over the oceans than over the land, (Figure 4B) with peak

485   frequencies of about 30 AAR days per year occurring over the subtropical trade wind regions,

486   Southern Ocean and northern Atlantic Ocean. In these regions, the total annual IAT is about

487   10000-20000 kg m^{-1}, and F_{AAR} is about ~ 20-30% in the subtropical regions, reaching a maximum

488   of ~50% over the Southern Ocean and the North Atlantic Ocean (Fig. 6B).

489   AARs for other species of aerosols can contribute to a maximum of 40% of the total annual

490   IAT over their major transport pathways. For example, the ~30 SU AAR days per year that

491   originate over China (Fig. 4C) transport ~30-40% of the total annual aerosol transport (~2500 kg

492   m^{-1}) over the northern Pacific Ocean. F_{AAR} associated with OC (BC) AARs is reaches a maximum

493   of 40% (30%) between the Congo basin and the tropical Atlantic Ocean. Over China and the

494   North Pacific Ocean, South Africa and the Southern/Indian Oceans, south China and the west

495   Pacific Ocean, and Amazon and the South Atlantic Ocean/Southern Ocean F_{AAR} can reach up to a

496 maximum of 40%. Higher F_{AAR} is also observed, despite low total annual IAT, over the northern

497 part of the Sahel region for both BC and OC AARs.

498 **4.5. AAR seasonality**
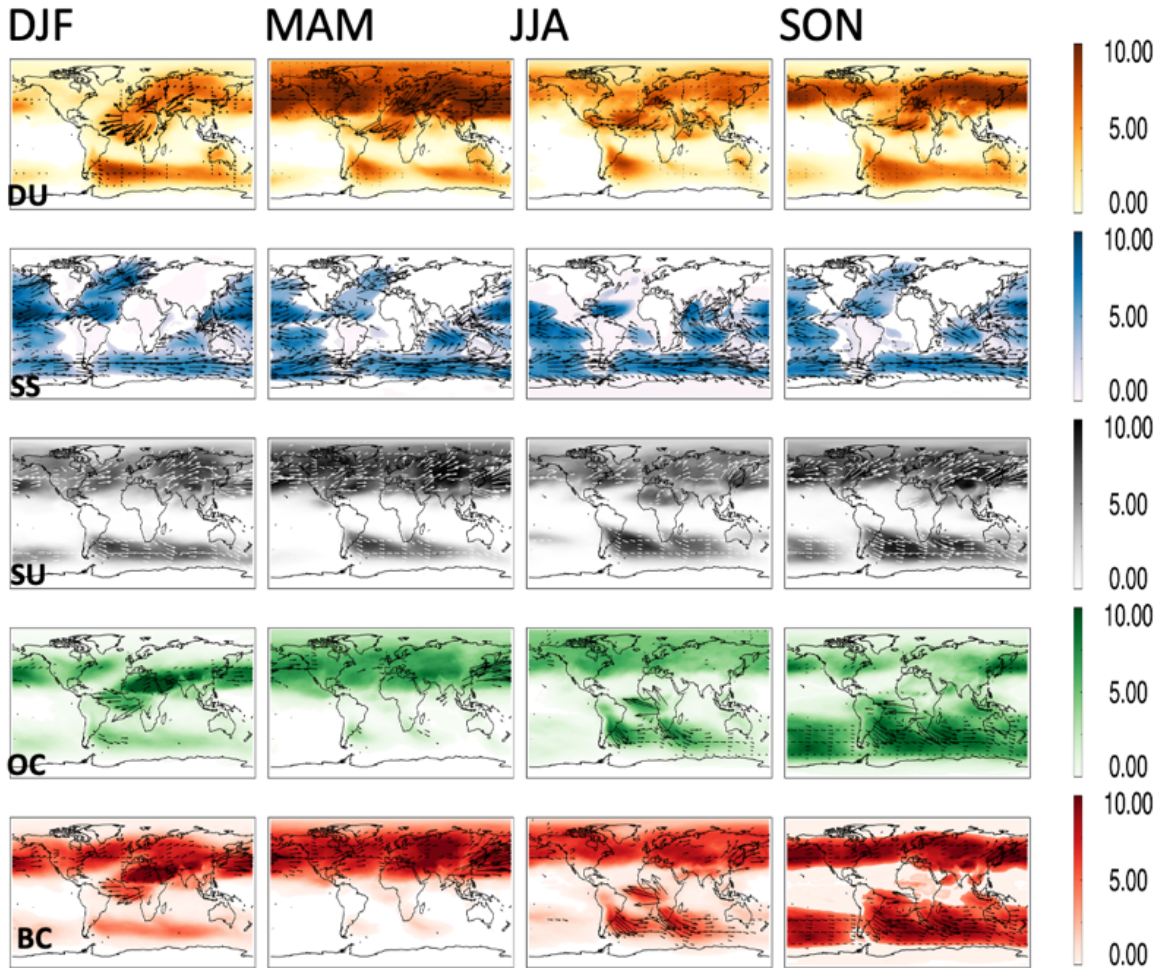
Figure 7. Seasonal variations of AAR frequency (days/season) and IAT (arrows) for five different species of aerosols.

499   Figure 7 shows AAR frequency along with the direction and magnitude of the mean AAR

500 IAT during four different seasons. DU AARs (shading) originate during all the seasons over the

501 Sahara Desert. DU AAR IAT (arrows) is higher during DJF and MAM over the Sahara Desert

502 owing to a stronger anticyclonic motion in the boreal winter and spring. The largest number of

503 DU AARs are generated during the MAM season when the DU IAT is the highest (Figure 1) and

504   widely spread across the Northern Hemisphere. In JJA and SON, DU AARs appear to have

505   lower IAT (shorter arrows), but are more frequent than in the DJF season. The frequency of SS

506   AARs also depends on the season. A higher number of SS AARs are detected over the eastern

507   Pacific Ocean and the west coast of the US, north Atlantic Ocean, and Europe in DJF and MAM.

508   In JJA, no SS AARs are detected over there. Over the Southern Ocean, SS AARs with large IAT

509   are more frequent during austral winter or MAM and JJA. In comparison, tropical SS AARs are

510   present year-round.

511   SU AARs in the Northern Hemisphere are more (less) frequent in MAM (JJA) and can be

512   related to the seasonal variations in IAT there (Figure 1). The frequency of occurrences of SU

513   AARs is higher during SON compared to DJF while their IAT values are larger in DJF. This

514   might be because of the readiness of sulfate aerosols to form CCNs and their hygroscopic nature.

515   The occurrences of intense AR-related precipitation in DJF over the extratropical region in the

516   Northern Hemisphere might cause scavenging and wet removal of SU aerosols when the AARs

517   and ARs coexist. A detailed investigation considering AR-AAR interactions is needed in future

518   studies to better understand the coexistence and influence of AARs and ARs.

519   Over the Congo rainforest, several OC AARs occur during its dry season (also when CA

520   IAT is high, Fig. 1). A similar frequency of occurrences of OC AARs is also observed during the

521   dry season over the Amazon rainforest. Many OC AARs occur east of China during the DJF and

522   MAM season when the IAT values are large over there (Fig. 1). Many BC and OC AARs are

523   generated over the global rainforests during their dry seasons.

524   **4.6 Basic characteristics of individual AARs and algorithm sensitivities**

525   In this section, we characterize basic features of AARs (Fig. 8), including those related to

526   geometry and IAT intensity and directions, and discuss and show the sensitivity of various AAR
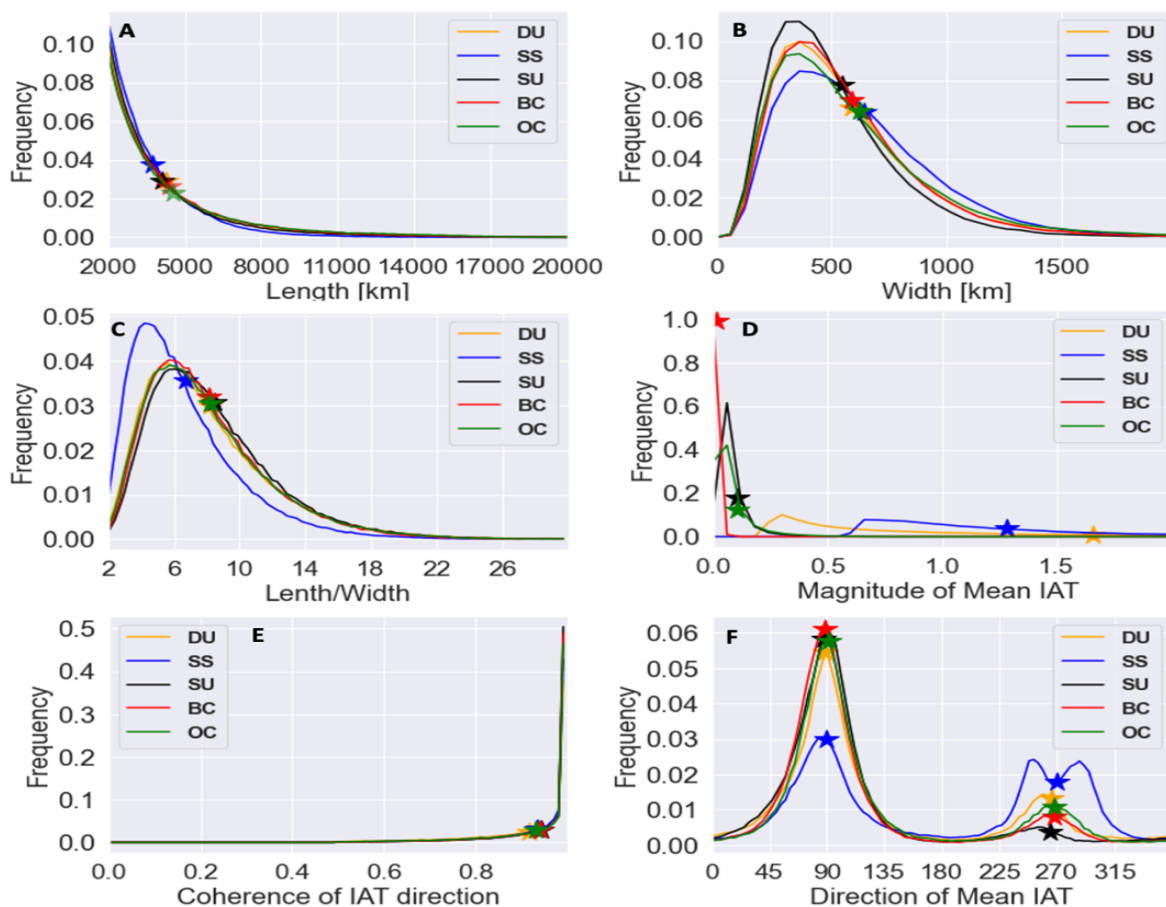
Figure 8. Histograms of characteristics of individual AARs. The "★" symbol denotes the mean. (A) Length. (B) Width. (C) Aspect ratio. (D) Magnitude of mean IAT. (E) Coherence of the IAT direction. (F) Direction of mean IAT.

527   features to algorithm specifications and thresholds (Fig. 9). Fig. 8A shows that the frequency of

528   AARs decreases monotonically as AAR length increases for all aerosol species. The mean

529   lengths of DU, SS, SU, OC, BC AARs are 4264 km, 3722 km, 4121 km, 4528 km, and 4378 km,

530   respectively. Fig. 8B shows that AAR widths exhibit a skewed distribution, unlike AAR lengths,

531   implying an optimum or common value for AAR widths around 400 km. The mean width of DU,

532   SS, SU, OC, BC AARs is 586 km, 642 km, 542 km, 625 km, and 589 km, respectively. When

533   considered together in the form of the aspect ratio of AARs, i.e., length/width ratio, the

534   distribution is also a skewed distribution (Fig. 8C). The lengths typically 7-8 times their widths

535   due to the skewness of the distribution. DU and SS AARs are the two species having the largest

536   object-mean IAT values (Fig. 8D). While on average, DU AARs have IAT ~ 1.65 and 1.3 x 10^{-3}

537   kg m^{-1}s^{-1}, respectively, SU, OC, and BC AARs have smaller IAT (Fig. 8D). Average object-

538   mean IAT for SU, OC, and BC AARs are 0.1, 0.1, and 0.016 x 10^{-3} kg m^{-1}s^{-1}, respectively. The

539   frequency of object-mean IAT for BC AARs decreases sharply and seldom reaches beyond 0.1 x

540   10^{-3} kg m^{-1}s^{-1}. SU (OC) AARs attain a maximum object-mean IAT values around 0.1 x 10^{-3} kg

541   m^{-1}s^{-1} with a maximum frequency of ~0.6 (0.4).

542   The coherence of IAT directions (Fig. 8E) is computed as a fraction of the number of grid

543   cells with IAT directed within 45° of the direction of the object-mean IAT to all the grid cells

544   within that AAR. A large value implies that a larger fraction of the grid cells has IAT directed in

545   the same overall direction as the AAR. AARs of all the species have the mean coherence of IAT

546   directions between 0.91 (DU) and 0.94 (SU). The distribution of the direction of the object-mean

547   IAT implies that the AARs are mostly directed in the zonal direction (Fig. 8F). Relative to North,

548   peak frequencies near 90° and between 250°- 310° imply that the AARs are either westerly or

549   easterly in nature. A few westerly AARs also transport aerosols in the northeastward (45°-90°)

550   and southeastward (90°-135°) directions. A wider peak between 250°- 310° implies that most of

551   the easterly AARs also have meridional components in the southwestward and northwestward

552   directions. The average values of object-mean IAT direction for all the species of AARs are ~90°

553   (westerly) and between 260-270° (easterly). These results show that the AARs mostly transport

554   aerosols in the zonal direction as compared to ARs that have notable transport of water vapor in

555   the meridional direction (Guan and Waliser, 2015).
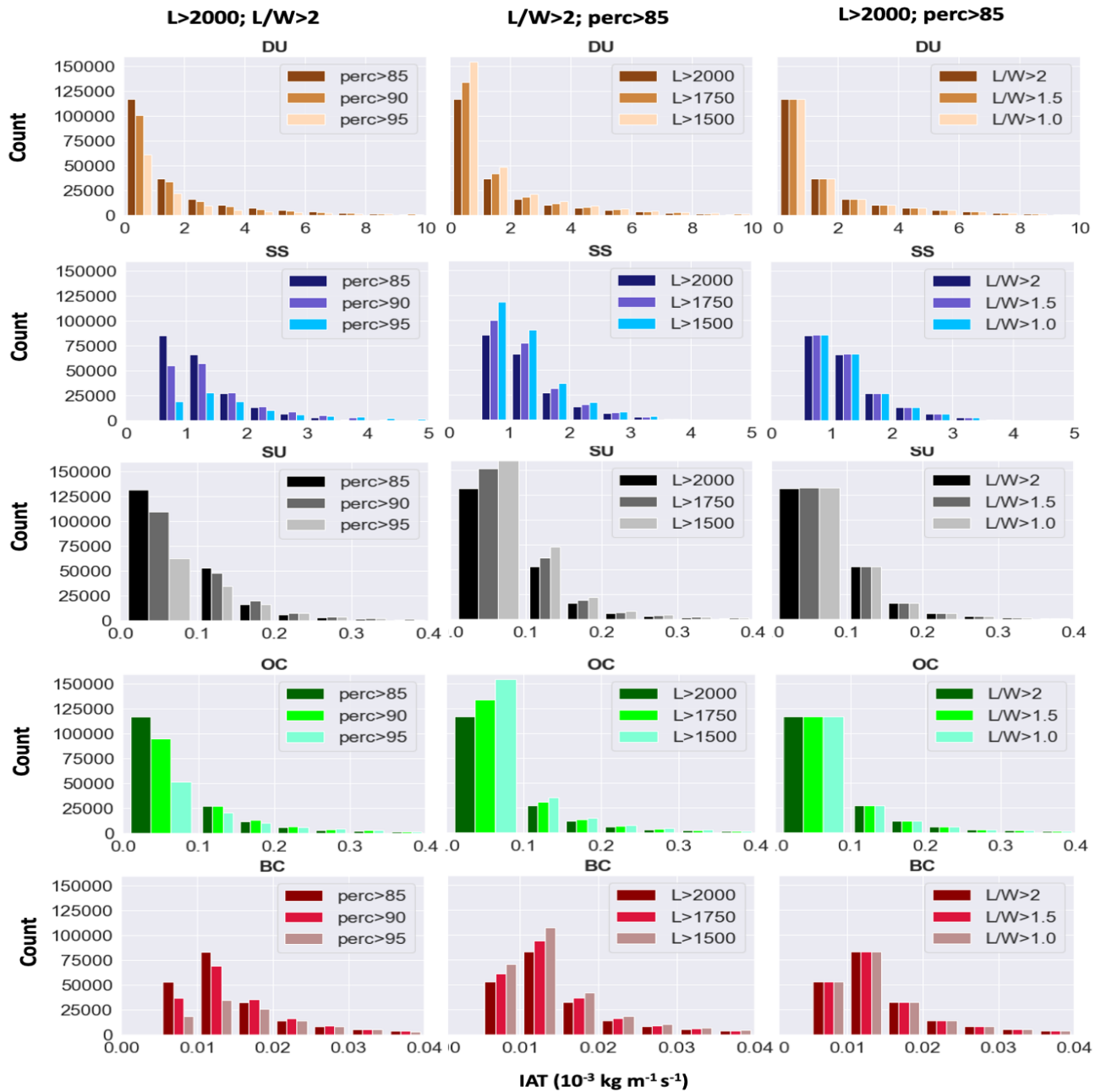
Figure 9. Sensitivity of AAR detection to threshold values used for three key parameters (corresponding to the three columns; see legend for the parameter being tested and the three values chosen for each test parameter) in the detection algorithm for five aerosol species (corresponding to the five rows; see panel title for the aerosol species). Shown are histograms of mean IAT of individual AARs detected. For example, the left column shows results based on perturbing the IAT percentile threshold (85th, 90th, and 95th percentiles) while keeping the length (2000 km) and aspect ratio (2) thresholds unchanged from the main analysis presented earlier.

556   Finally, Figure 9 shows the sensitivity of AAR detection in our algorithm to three primary

557 thresholds that define the geometry (length and aspect ratio) and grid-wise IAT limits (to identify

558 the extreme transport) of AARs. The results presented above in this study are based on a length

559 limit of 2000 km, aspect ratio limit of 2, and a pixel-wise IAT limit of the 85th percentile.

560 Keeping the length and aspect ratio limits fixed, while increasing the IAT limit to the 90th and

561 95th percentile values, yields fewer number of AARs detected (top row). On the other hand,

562 relaxing the length limit to 1750 km and 1500 km greatly increases the number of AARs

563 detected (middle row). Relaxing the aspect ratio limit to 1.5 and 1 does not significantly alter the

564 number of AARs detected, suggesting that the other limits applied (such as length greater than

565 2000 km) already effectively removes IAT objects that are not elongated. It appears from Figure

566 9 that grid-wise IAT thresholds pose a large sensitivity to AARs detection as the number of

567 AARs detected is reduced roughly by half as we increase that threshold to the 95th percentile

568 from the 85th percentile used in our main analysis.

569   Figure 10 shows the sensitivity of the average global area coverage of all AARs to AAR

570 algorithm parameters. Each bar represents the area-weighted global mean AAR frequency or a

571 spatial-temporal measure of the amount of time/space that there is an AAR. Annually, AARs

572 cover 3.42 % of the global area, respectively. Upon relaxing the length limits to 1750 (1500) km

573 increases the number of detections of AARs, thus the areal coverage of AARs increases to 3.56%

574 (3.76%). On the other hand, increasing the pixel-wise IAT limit to 90th and 95th percentile

575 reduces the areal coverage to 2.44% and 1.13%, respectively. Relaxing the aspect ratio doesn't

576 have any impact on AAR's areal coverage. ARs, on the other hand, account for ~2% more of the

577 Earth's surface area than AARs (not shown), likely because the filter based on object-mean

578 IVT direction in the AR algorithm preferentially filtered out smaller objects compared to the

579 revised filter in the AAR algorithm based on IAT magnitude.
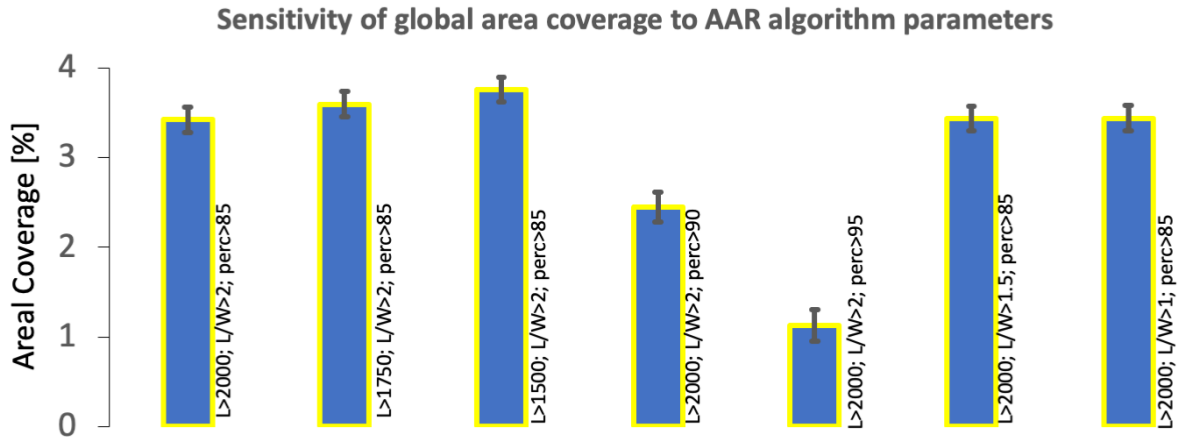
Figure 10. Sensitivity of AARs' and ARs' global area coverage to threshold values used for three key parameters in the detection algorithm. For each species of AARs, the first bar shows the average global area coverage for the length limit >2000, aspect ratio > 2, and the pixel-wise IAT threshold >85%. Next two bars show the areal coverage after relaxing the length limit to 1750 and 1500 km. The fourth and the fifth bar shows the areal coverage after increasing the pixel-wise IAT limit to 90th and 95th percentile. The last two bars show the areal coverage after relaxing the aspect ratio to 1.5 and 1. Standard deviations show the variations in areal coverage by different species.

580

5. Conclusions

Using a newly developed AAR algorithm (Chakraborty et al, 2021a) based on the widely used

AR detection algorithm (Guan and Waliser, 2015), we examine a number of important details

about AARs that were not explored in Chakraborty et al. (2021a). This includes AAR seasonal

variations in frequency and transport values (Fig. 7), the fraction of total annual aerosol transport

account for by AARs (Fig. 6), a characterization of their vertical profiles (Fig. 5), relation to the

pattern of surface emissions (Fig. 2), along with a number of basic characteristics and

distributions for quantities such as AAR length, aspect ratio, object-mean IAT, the coherence of

the direction of IAT (Fig. 8), and sensitivities of the algorithm to the thresholds chosen for three

key parameters (Fig.9). To our knowledge, this study significantly advances the understanding of

591   global aerosol transport events. This study is the first to provide a common detection and

592   analytical basis for studying extreme transport events, heavily leveraging the heritage and

593   methodologies by the (water vapor) atmospheric river community. Moreover, this study

594   identifies the extreme transport events by selecting grid cells with IAT values greater than the

595   85th percentile of their climatological values and retaining the stronger 50% of those objects

596   detected based on the object-mean IAT values. This study creates a database of the AAR events

597   between 1997-2014 that will be expanded till 2020 and will provide a valuable platform for

598   aerosol transport-related research including their impacts on the climate and air quality.

599   Furthermore, the algorithm developed to detect AARs can be used to detect the real-time AAR

600   events using the nature run of the GOES FP system that provides analyses and forecasts

601   produced in real-time, using the most recent validated GEOS system

602   (https://gmao.gsfc.nasa.gov/GMAO_products/NRT_products.php).

603   The global total annual transport by All and AAR events are inhomogeneous in terms of their

604   geographic distributions. F_{AAR} varies between 0-40% for SU, OC, and BC AARs, between 0-80%

605   for DU AARs, and between 0-50% for SS AARs over various regions of the world. Our results

606   show that on average, 30-40 SU, BC, and OC AAR days every year are responsible for a

607   maximum of 30-40% of total annual aerosol transport for a given aerosol species over certain

608   major transport pathways around the globe. Over the major transport pathways of the SS (DU)

609   AARs, F_{AAR} can reach up to a maximum of 50 (80) % of the total annual aerosol transport of the

610   respective species. The inhomogeneous nature of AARs' spatial distribution and fractional

611   transport out of the annual total suggest a plausible impact of the AARs on the meridional

612   temperature gradient. The attenuation of solar energy by AARs might impact the surface

613   temperature, thus can alter the meridional temperature gradient and the thermal winds. Further

614 analysis will be conducted in the future to delineate the impacts of AARs on the global weather

615 and climate.

616   The major transport pathways by AARs are also identified in our algorithm for each of the

617 aerosol species. The source of AARs is consistent with the major aerosol emission regions of the

618 world. DU aerosols are mostly originated from the global deserts and their frequency is higher

619 during boreal autumn and spring. SS AARs are mostly located over the global oceans and carry

620 the footprint of the storms. In the midlatitudes their frequency and intensity increase during the

621 boreal (austral) winter in the Northern (Southern) Hemisphere. Tropical SS AARs are more

622 frequent, but their magnitude of aerosol transport and contribution to the annual aerosol transport

623 is less. A further investigation is needed to understand if/how tropical cyclones and midlatitude

624 storms impact SS AARs differently. CA AARs are generated over the region where biomass

625 burning is more common like India and China. CA AARs that originate from the global boreal

626 and tropical rainforests have the highest frequency as well as intensity during their dry seasons,

627 but are mostly absent or exist with a reduced frequency during their wet seasons. SU AARs are

628 present year around in the northern hemisphere with a peak frequency and intensity during the

629 dry periods-boreal spring (MAM) and autumn (SON). The frequency of SU AARs occurrences

630 reduces during the boreal summer and winter, presumably due to the summertime convective

631 precipitation events and wintertime synoptic storms. Overall, regions with frequent AAR

632 activities include the Sahara Desert to Caribbean and Europe for DU AARs, a circumpolar

633 transport around the midlatitude region in the northern hemisphere for all but SS AARs, global

634 oceans and midlatitude storm tracks over the global ocean for SS AARs, global rainforests for

635 BC and OC AARs, and from South America and Africa to the Southern Ocean for DU, BC, OC,

636 and SU AARs.

637   We have also examined the vertical structure of aerosol mixing ratio and wind inside AARs.

638   Over most of the major pathways, aerosol mixing ratio and flux values decrease with height. A

639   higher aerosol mass mixing ratio inside AARs is observed below the 700 hPa over most of the

640   regions and thus, may have a strong implication on the low cloud cover and surface irradiance.

641   Such an interaction can be complex since shallow clouds also have cooling effects as most of the

642   aerosol species do. Understanding such an interaction between shallow clouds and AARs and

643   their impacts on the cooling effect warrants further investigation. The aerosol mixing ratio (wind

644   speed) appears to contribute a large fraction of IAT below (above) 700 hPa. However, AARs

645   generated from the African continent are the exceptions. Signatures of AEJ-N on DU AARs

646   taking off the Sahara Desert and AEJ-S on BC/OC AARs originated from the Congo basin are

647   observed. Both the aerosol mixing ratio and wind speed appear to peak around 600-700 hPa,

648   leading to a higher IAT at the level. The fact that aerosols are lifted up and attain a peak mass

649   flux around the 700 hPa for AARs generated from the African continent might have a strong

650   influence on the wet season onset and rainfall mechanisms over there (Chakraborty et al.,

651   2021b). We acknowledge a source of uncertainty in the aerosol mass mixing ratio and IAT

652   profiles shown in this study from the MERRA-2 data since MERRA-2 aerosol vertical

653   distribution is also not constrained by satellite-based lidar observations. A recent study found

654   that comparison to the CALIOPO VFM data detects a greater occurrence of DU aerosols in

655   MERRA-2 due to errors in MERRAero aerosol speciation (Nowottnick et al., 2015). In a future

656   study, an in-depth analysis will be performed using the observation from the ground-based and

657   air borne measurements (wherever available) and CALIPSO. For example, ORACLES mission

658   and Cloud-Aerosol Lidar and Infrared Pathfinder Satellite Observation can be used to to study

659 the subsidence that depresses the plumes once they reach the Atlantic Ocean off the west African

660 Coast (Das et al., 2017).

661   AAR frequency of occurrence decreases monotonically with its length with the mean around

662 4000 km. However, AAR width and aspect ratio show a skewed distribution. AAR length is, on

663 average, 6-8 times the width. DU and SS AARs carry a larger amount of aerosol mass as

664 compared to SU, OC, and BC aerosols. More than 90% of all the grid cells within an individual

665 AAR have IAT directed in the same overall direction of the AAR, showing that the transport

666 occurring inside an individual AAR is largely coherent in direction. AARs are mostly oriented in

667 the zonal direction. A peak frequency of the direction of object-mean IAT is observed between

668 45°-135° (westerly AARs) or 225°-315° (easterly AARs). Large mean width and length (Figure

669 8A and 8B) of AARs imply that AARs have a significant amount of areal cover. AARs also

670 transport a higher aerosol mass mixing ratio, located mostly in the lower troposphere, to regions

671 far from their sources – often intercontinental 20-40 days per year on average. Our findings, thus,

672 indicate the necessity of exploring the impacts of AARs on human health since smoke as well as

673 dust particles and the secondary aerosol particles that can be generated over the AAR lifetime

674 might have a huge impact on human health, especially on lungs. The algorithm shows little to no

675 sensitivity to the aspect ratio limit chosen, but notable influence of the length limit, and strongest

676 influence of the IAT percentile limit on the detection result.

677   This study points out the necessity to analyze and investigate the impact of AARs on climate

678 and air quality. The fact that AARs can carry a greater number of aerosol particles through a

679 narrow pathway and probably can contain more aerosol particles than a moderate-high AOD

680 region suggests that their impact on radiative forcing and cloud microphysics can be stronger

681 than that have been reported and investigated so far in the literature. We have not addressed the

682   role of climate modulation on AAR activity and characteristics. Events like El Niño, La Niña,

683   Pacific Decadal Oscillation, North American Subtropical High, Madden-Julian Oscillations can

684   have a significant influence on AARs and will be addressed in future studies. A further

685   investigation is needed on the AR and AAR interaction and how ARs and cyclonic activities

686   modulate AARs in the midlatitude during the winter season of each hemisphere.

687   **Author Contribution:**

688   SC, BG, DW, and AMS designed the research and wrote the paper. SC analyzed the data.

689   **Competing Interests:**

690   The authors have no competing interests.

691   **Data and Code Availability**

692   All satellite data used in this study can be downloaded at the EOSDIS Distributed Active

693   Archive Centers (DAACs) at https://earthdata.nasa.gov/eosdis/daacs. References about the

694   datasets have been provided in the Data section (Sect. 2). Please contact the corresponding author

695   for any questions about how to download the data that are publicly available and codes written in

696   IDL and Python. The AAR data set will be made publicly available after the publication. The AAR

697   code is available from B.G. on request.

698   **Acknowledgements:**

699   This work was supported by the National Aeronautics and Space Administration. The

700   contribution of S.C. and D.W. was carried out on behalf of the Jet Propulsion Laboratory,

701   California Institute of Technology, under a contract with NASA. All the data are publicly

702   available and free to download. Please see reference section for the citations to all the data sets

703   used in this study. Also, details about the dataset have been included in the supplementary

704   section.

References

Abdalmogith, S. S. and Harrison, R. M.: The use of trajectory cluster analysis to examine the long-range transport of secondary inorganic aerosol in the UK, 39, 6686–6695, https://doi.org/https://doi.org/10.1016/j.atmosenv.2005.07.059, 2005.

Ackermann, I. J., Hass, H., Memmesheimer, M., Ziegenbein, C., and Ebel, A.: The parametrization of the sulfate-nitrate-ammonia aerosol system in the long-range transport model EURAD, 57, 101–114, 1995.

Adebiyi, A. A. and Zuidema, P.: The role of the southern African easterly jet in modifying the southeast Atlantic aerosol and cloud environments, https://doi.org/10.1002/qj.2765, 2016.

Andreae, M. O. and Rosenfeld, D.: Aerosol-cloud-precipitation interactions. Part 1. The nature and sources of cloud-active aerosols, https://doi.org/10.1016/j.earscirev.2008.03.001, 2008.

Bertschi, I. T., Jaffe, D. A., Jaeglé, L., Price, H. U., and Dennison, J. B.: PHOBEA/ITCT 2002 airborne observations of transpacific transport of ozone, CO, volatile organic compounds, and aerosols to the northeast Pacific: Impacts of Asian anthropogenic and Siberian boreal fire emissions, 109, 2004a.

Bertschi, I. T., Jaffe, D. A., Jaeglé, L., Price, H. U., and Dennison, J. B.: PHOBEA/ITCT 2002 airborne observations of transpacific transport of ozone, CO, volatile organic compounds, and aerosols to the northeast Pacific: Impacts of Asian anthropogenic and Siberian boreal fire emissions, 109, 2004b.

Bister, M. and Kulmala, M.: Anthropogenic aerosols may have increased upper tropospheric humidity in the 20th century, https://doi.org/10.5194/acp-11-4577-2011, 2011.

Buchard, V., Randles, C. A., da Silva, A. M., Darmenov, A., Colarco, P. R., Govindaraju, R., Ferrare, R., Hair, J., Beyersdorf, A. J., Ziemba, L. D., and Yu, H.: The MERRA-2 aerosol reanalysis, 1980 onward. Part II: Evaluation and case studies, https://doi.org/10.1175/JCLI-D-16-0613.1, 2017.

Chakraborty, S., Fu, R., Massie, S. T., and Stephens, G.: Relative influence of meteorological conditions and aerosols on the lifetime of mesoscale convective systems, Proc Natl Acad Sci U S A, https://doi.org/10.1073/pnas.1601935113, 2016.

Chakraborty, S., Fu, R., Rosenfeld, D., and Massie, S. T.: The Influence of Aerosols and Meteorological Conditions on the Total Rain Volume of the Mesoscale Convective Systems Over Tropical Continents, 45, 13,13-99,106, https://doi.org/10.1029/2018GL080371, 2018.

Chakraborty, S., Guan, B., Waliser, D. E., da Silva, A. M., Uluatam, S., and Hess, P.: Extending the Atmospheric River Concept to Aerosols: Climate and Air Quality Impacts, https://doi.org/10.1029/2020GL091827, 2021a.

Chakraborty, S., Jiang, J. H., Su, H., and Fu, R.: On the Role of Aerosol Radiative Effect in the Wet Season Onset Timing over the Congo Rainforest during Boreal Autumn, 2021, 1–27, https://doi.org/10.5194/acp-2020-1138, 2021b.

Chapman, W. E., Subramanian, A. C., Delle Monache, L., Xie, S. P., and Ralph, F. M.: Improving Atmospheric River Forecasts With Machine Learning, https://doi.org/10.1029/2019GL083662, 2019.

Chen, T.-F., Chang, K.-H., and Tsai, C.-Y.: Modeling direct and indirect effect of long range transport on atmospheric PM2. 5 levels, 89, 1–9, 2014.

Chylek, P. and Wong, J.: Effect of absorbing aerosols on global radiation budget, https://doi.org/10.1029/95GL00800, 1995.

750 Cook, K. H.: Generation of the African easterly jet and its role in determining West African
751 precipitation, https://doi.org/10.1175/1520-0442(1999)012<1165:GOTAEJ>2.0.CO;2, 1999.
752 Dai, Q., Bi, X., Song, W., Li, T., Liu, B., Ding, J., Xu, J., Song, C., Yang, N., Schulze, B. C.,
753 Zhang, Y., Feng, Y., and Hopke, P. K.: Residential coal combustion as a source of primary
754 sulfate in Xi'an, China, https://doi.org/10.1016/j.atmosenv.2018.10.002, 2019.
755 Das, S., Harshvardhan, H., Bian, H., Chin, M., Curci, G., Protonotariou, A. P., Mielonen, T.,
756 Zhang, K., Wang, H., and Liu, X.: Biomass burning aerosol transport and vertical distribution
757 over the South African-Atlantic region, https://doi.org/10.1002/2016JD026421, 2017.
758 Dhana Laskhmi, D. and Satyanarayana, A. N. V.: Climatology of landfalling atmospheric Rivers
759 and associated heavy precipitation over the Indian coastal regions,
760 https://doi.org/10.1002/joc.6540, 2020.
761 Edwards, T. K., Smith, L. M., and Stechmann, S. N.: Atmospheric rivers and water fluxes in
762 precipitating quasi-geostrophic turbulence, https://doi.org/10.1002/qj.3777, 2020.
763 Fan, J., Leung, L. R., DeMott, P. J., Comstock, J. M., Singh, B., Rosenfeld, D., Tomlinson, J.
764 M., White, A., Prather, K. A., and Minnis, P.: Aerosol impacts on California winter clouds and
765 precipitation during CalWater 2011: local pollution versus long-range transported dust, 14, 81–
766 101, 2014.
767 Fan, J., Wang, Y., Rosenfeld, D., and Liu, X.: Review of aerosol-cloud interactions:
768 Mechanisms, significance, and challenges, https://doi.org/10.1175/JAS-D-16-0037.1, 2016.
769 Fast, J. D., Allan, J., Bahreini, R., Craven, J., Emmons, L., Ferrare, R., Hayes, P. L., Hodzic, A.,
770 Holloway, J., and Hostetler, C.: Modeling regional aerosol and aerosol precursor variability over
771 California and its sensitivity to emissions and long-range transport during the 2010 CalNex and
772 CARES campaigns, 14, 10013–10060, 2014a.
773 Fast, J. D., Allan, J., Bahreini, R., Craven, J., Emmons, L., Ferrare, R., Hayes, P. L., Hodzic, A.,
774 Holloway, J., and Hostetler, C.: Modeling regional aerosol and aerosol precursor variability over
775 California and its sensitivity to emissions and long-range transport during the 2010 CalNex and
776 CARES campaigns, 14, 10013–10060, 2014b.
777 Febo, A., Guglielmi, F., Manigrasso, M., Ciambottini, V., and Avino, P.: Local air pollution and
778 long–range mass transport of atmospheric particulate matter: A comparative study of the
779 temporal evolution of the aerosol size fractions, 1, 141–146, 2010.
780 Froyd, K. D., Murphy, D. M., Sanford, T. J., Thomson, D. S., Wilson, J. C., Pfister, L., and Lait,
781 L.: Aerosol composition of the tropical upper troposphere, https://doi.org/10.5194/acp-9-4363-
782 2009, 2009.
783 Garrett, T. J. and Hobbs, P. v: Long-range transport of continental aerosols over the Atlantic
784 Ocean and their effects on cloud structures, 52, 2977–2984, 1995.
785 Gelaro, R., McCarty, W., Suárez, M. J., Todling, R., Molod, A., Takacs, L., Randles, C. A.,
786 Darmenov, A., Bosilovich, M. G., Reichle, R., Wargan, K., Coy, L., Cullather, R., Draper, C.,
787 Akella, S., Buchard, V., Conaty, A., da Silva, A. M., Gu, W., Kim, G.-K., Koster, R., Lucchesi,
788 R., Merkova, D., Nielsen, J. E., Partyka, G., Pawson, S., Putman, W., Rienecker, M., Schubert,
789 S. D., Sienkiewicz, M., and Zhao, B.: The Modern-Era Retrospective Analysis for Research and
790 Applications, Version 2 (MERRA-2), 30, 5419–5454, https://doi.org/10.1175/JCLI-D-16-0758.1,
791 2017.
792 Gibson, P. B., Waliser, D. E., Guan, B., Deflorio, M. J., Ralph, F. M., and Swain, D. L.: Ridging
793 associated with Drought across the Western and Southwestern United States: Characteristics,
794 trends, and predictability sources, https://doi.org/10.1175/JCLI-D-19-0439.1, 2020.

795 Global Modeling and Assimilation Office (GMAO): MERRA-2 tavg1_2d_aer_Nx: 2d,1-
796 Hourly,Time-averaged,Single-Level,Assimilation,Aerosol Diagnostics V5.12.4, Goddard Earth
797 Sciences Data and Information Services Center (GES DISC), Greenbelt, MD, USA,
798 https://doi.org/10.5067/KLICLTZ8EM9D, 2015a.
799 Global Modeling and Assimilation Office (GMAO): MERRA-2 tavgU_2d_adg_Nx:
800 2d,diurnal,Time-averaged,Single-Level,Assimilation,Aerosol Diagnostics (extended) V5.12.4,
801 Greenbelt, MD, USA, 2015b.
802 Gohm, A., Harnisch, F., Vergeiner, J., Obleitner, F., Schnitzhofer, R., Hansel, A., Fix, A.,
803 Neininger, B., Emeis, S., and Schäfer, K.: Air pollution transport in an Alpine valley: Results
804 from airborne and ground-based observations, Boundary Layer Meteorol, 131, 441–463, 2009a.
805 Gohm, A., Harnisch, F., Vergeiner, J., Obleitner, F., Schnitzhofer, R., Hansel, A., Fix, A.,
806 Neininger, B., Emeis, S., and Schäfer, K.: Air pollution transport in an Alpine valley: Results
807 from airborne and ground-based observations, Boundary Layer Meteorol, 131, 441–463, 2009b.
808 Gross, A. and Baklanov, A.: Aerosol Production in the Marine Boundary Layer Due to
809 Emissions from DMS: Study Based on Theoretical Scenarios Guided by Field Campaign Data,
810 in: Air Pollution Modeling and Its Application XVII, https://doi.org/10.1007/978-0-387-68854-
811 1_31, 2007.
812 Gu, L., Baldocchi, D. D., Wofsy, S. C., Munger, J. W., Michalsky, J. J., Urbanski, S. P., and
813 Boden, T. A.: Response of a Deciduous Forest to the Mount Pinatubo Eruption: Enhanced
814 Photosynthesis, Science (1979), 299, 2035–2038, https://doi.org/10.1126/science.1078366, 2003.
815 Guan, B. and Waliser, D. E.: Detection of atmospheric rivers: Evaluation and application of an
816 algorithm for global studies, https://doi.org/10.1002/2015JD024257, 2015.
817 Guan, B. and Waliser, D. E.: Tracking Atmospheric Rivers Globally: Spatial Distributions and
818 Temporal Evolution of Life Cycle Characteristics, https://doi.org/10.1029/2019JD031205, 2019.
819 Guan, B., Waliser, D. E., and Martin Ralph, F.: An intercomparison between reanalysis and
820 dropsonde observations of the total water vapor transport in individual atmospheric rivers,
821 https://doi.org/10.1175/JHM-D-17-0114.1, 2018.
822 Guan, B., Waliser, D. E., and Ralph, F. M.: A multimodel evaluation of the water vapor budget
823 in atmospheric rivers, Ann N Y Acad Sci, https://doi.org/10.1111/nyas.14368, 2020.
824 Gupta, P. and Christopher, S. A.: Particulate matter air quality assessment using integrated
825 surface, satellite, and meteorological products: 2. A neural network approach,
826 https://doi.org/10.1029/2008JD011497, 2009.
827 Han, L., Cheng, S., Zhuang, G., Ning, H., Wang, H., Wei, W., and Zhao, X.: The changes and
828 long-range transport of PM2. 5 in Beijing in the past decade, 110, 186–195, 2015.
829 Huang, Y., Dickinson, R. E., and Chameides, W. L.: Impact of aerosol indirect effect on surface
830 temperature over East Asia, Proc Natl Acad Sci U S A,
831 https://doi.org/10.1073/pnas.0504428103, 2006.
832 Huning, L. S., Guan, B., Waliser, D. E., and Lettenmaier, D. P.: Sensitivity of Seasonal Snowfall
833 Attribution to Atmospheric Rivers and Their Reanalysis-Based Detection,
834 https://doi.org/10.1029/2018GL080783, 2019.
835 IPCC: Climate Change 2013: The Physical Science Basis. Contribution of Working Group I to
836 the Fifth Assessment Report of the Intergovernmental Panel on Climate Change, 1535 pp.,
837 https://doi.org/doi:10.1017/CBO9781107415324, 2013a.
838 IPCC: Working Group I Contribution to the IPCC Fifth Assessment Report, Climate Change
839 2013: The Physical Science Basis, AR5, 2014,
840 https://doi.org/10.1017/CBO9781107415324.Summary, 2013b.

841 Jennrich, G. C., Furtado, J. C., Basara, J. B., and Martin, E. R.: Synoptic Characteristics of 14-
842 Day Extreme Precipitation Events across the United States, https://doi.org/10.1175/JCLI-D-19-
843 0563.1, 2020.
844 Keil, A. and Haywood, J. M.: Solar radiative forcing by biomass burning aerosol particles during
845 SAFARI 2000: A case study based on measured aerosol and cloud properties,
846 https://doi.org/10.1029/2002jd002315, 2003.
847 Khain, A. P., BenMoshe, N., and Pokrovsky, A.: Factors determining the impact of aerosols on
848 surface precipitation from clouds: An attempt at classification,
849 https://doi.org/10.1175/2007JAS2515.1, 2008.
850 Kim, D. and Ramanathan, V.: Solar radiation budget and radiative forcing due to aerosols and
851 clouds, https://doi.org/10.1029/2007JD008434, 2008.
852 Kim, Y. J., Woo, J.-H., Ma, Y.-I., Kim, S., Nam, J. S., Sung, H., Choi, K.-C., Seo, J., Kim, J. S.,
853 and Kang, C.-H.: Chemical characteristics of long-range transport aerosol at background sites in
854 Korea, 43, 5556–5566, 2009.
855 Kindap, T., Unal, A., Chen, S.-H., Hu, Y., Odman, M. T., and Karaca, M.: Long-range aerosol
856 transport from Europe to Istanbul, Turkey, 40, 3536–3547,
857 https://doi.org/https://doi.org/10.1016/j.atmosenv.2006.01.055, 2006a.
858 Kindap, T., Unal, A., Chen, S.-H., Hu, Y., Odman, M. T., and Karaca, M.: Long-range aerosol
859 transport from Europe to Istanbul, Turkey, 40, 3536–3547,
860 https://doi.org/https://doi.org/10.1016/j.atmosenv.2006.01.055, 2006b.
861 Knohl, A. and Baldocchi, D. D.: Effects of diffuse radiation on canopy gas exchange processes
862 in a forest ecosystem, 113, https://doi.org/https://doi.org/10.1029/2007JG000663, 2008.
863 Li, Z., Guo, J., Ding, A., Liao, H., Liu, J., Sun, Y., Wang, T., Xue, H., Zhang, H., and Zhu, B.:
864 Aerosol and boundary-layer interactions and impact on air quality,
865 https://doi.org/10.1093/nsr/nwx117, 2017a.
866 Li, Z., Guo, J., Ding, A., Liao, H., Liu, J., Sun, Y., Wang, T., Xue, H., Zhang, H., and Zhu, B.:
867 Aerosol and boundary-layer interactions and impact on air quality,
868 https://doi.org/10.1093/nsr/nwx117, 2017b.
869 Lohmann, U. and Feichter, J.: Can the direct and semi-direct aerosol effect compete with the
870 indirect effect on a global scale?, https://doi.org/10.1029/2000GL012051, 2001.
871 Markowicz, K. M., Chilinski, M. T., Lisok, J., Zawadzka, O., Stachlewska, I. S., Janicka, L.,
872 Rozwadowska, A., Makuch, P., Pakszys, P., Zielinski, T., Petelski, T., Posyniak, M., Pietruczuk,
873 A., Szkop, A., and Westphal, D. L.: Study of aerosol optical properties during long-range
874 transport of biomass burning from Canada to Central Europe in July 2013, 101, 156–173,
875 https://doi.org/https://doi.org/10.1016/j.jaerosci.2016.08.006, 2016.
876 Martin, R. V.: Satellite remote sensing of surface air quality,
877 https://doi.org/10.1016/j.atmosenv.2008.07.018, 2008.
878 May, N. W., Quinn, P. K., McNamara, S. M., and Pratt, K. A.: Multiyear study of the
879 dependence of sea salt aerosol on wind speed and sea ice conditions in the coastal Arctic,
880 https://doi.org/10.1002/2016JD025273, 2016.
881 McComiskey, A. and Feingold, G.: Quantifying error in the radiative forcing of the first aerosol
882 indirect effect, https://doi.org/10.1029/2007GL032667, 2008.
883 Mishra, A. K., Koren, I., and Rudich, Y.: Effect of aerosol vertical distribution on aerosol-
884 radiation interaction: A theoretical prospect, Heliyon,
885 https://doi.org/10.1016/j.heliyon.2015.e00036, 2015.

886 Mori, I., Nishikawa, M., Tanimura, T., and Quan, H.: Change in size distribution and chemical
887 composition of kosa (Asian dust) aerosol during long-range transport, 37, 4253–4263, 2003.
888 Nash, D. and Carvalho, L.: Brief Communication: An Electrifying Atmospheric River:
889 Understanding the Thunderstorm Event in Santa Barbara County during March 2019,
890 https://doi.org/10.5194/nhess-2019-342, 2019.
891 Niyogi, D., Chang, H.-I., Saxena, V. K., Holt, T., Alapaty, K., Booker, F., Chen, F., Davis, K. J.,
892 Holben, B., Matsui, T., Meyers, T., Oechel, W. C., Pielke Sr., R. A., Wells, R., Wilson, K., and
893 Xue, Y.: Direct observations of the effects of aerosol loading on net ecosystem CO_2 exchanges
894 over different landscapes, 31, https://doi.org/https://doi.org/10.1029/2004GL020915, 2004.
895 Prospero, J. M.: Long-term measurements of the transport of African mineral dust to the
896 southeastern United States: Implications for regional air quality, 104, 15917–15927, 1999.
897 Prospero, J. M., Olmez, I., and Ames, M.: Al and Fe in PM 2.5 and PM 10 suspended particles in
898 south-central Florida: The impact of the long range transport of African mineral dust, 125, 291–
899 317, 2001.
900 Qin, K., Wu, L., Wong, M. S., Letu, H., Hu, M., Lang, H., Sheng, S., Teng, J., Xiao, X., and
901 Yuan, L.: Trans-boundary aerosol transport during a winter haze episode in China revealed by
902 ground-based Lidar and CALIPSO satellite, Atmos Environ, 141, 20–29, 2016a.
903 Qin, K., Wu, L., Wong, M. S., Letu, H., Hu, M., Lang, H., Sheng, S., Teng, J., Xiao, X., and
904 Yuan, L.: Trans-boundary aerosol transport during a winter haze episode in China revealed by
905 ground-based Lidar and CALIPSO satellite, Atmos Environ, 141, 20–29, 2016b.
906 Rajeev, K., Ramanathan, V., and Meywerk, J.: Regional aerosol distribution and its long-range
907 transport over the Indian Ocean, 105, 2029–2043, 2000a.
908 Rajeev, K., Ramanathan, V., and Meywerk, J.: Regional aerosol distribution and its long-range
909 transport over the Indian Ocean, 105, 2029–2043, 2000b.
910 Ralph, F. M., Dettinger, M. D., Rutz, J. J., and Waliser, D. E.: Atmospheric Rivers, 2020th ed.,
911 https://doi.org/10.1007/978-3-030-28906-5, n.d.
912 Ramanathan, V., Li, F., Ramana, M. v, Praveen, P. S., Kim, D., Corrigan, C. E., Nguyen, H.,
913 Stone, E. A., Schauer, J. J., and Carmichael, G. R.: Atmospheric brown clouds: Hemispherical
914 and regional variations in long-range transport, absorption, and radiative forcing, 112, 2007.
915 Randles, C. A., da Silva, A. M., Buchard, V., Colarco, P. R., Darmenov, A., Govindaraju, R.,
916 Smirnov, A., Holben, B., Ferrare, R., Hair, J., Shinozuka, Y., and Flynn, C. J.: The MERRA-2
917 aerosol reanalysis, 1980 onward. Part I: System description and data assimilation evaluation,
918 https://doi.org/10.1175/JCLI-D-16-0609.1, 2017.
919 Rosenfeld, D., Lohmann, U., Raga, G. B., O'Dowd, C. D., Kulmala, M., Fuzzi, S.,
920 Reissell, A., and Andreae, M. O.: Flood or Drought: How Do Aerosols Affect Precipitation?,
921 Science (1979), 321, 1309 LP – 1313, https://doi.org/10.1126/science.1160606, 2008.
922 Rosenfeld, D., Wood, R., Donner, L. J., and Sherwood, S. C.: Aerosol Cloud-Mediated Radiative
923 Forcing: Highly Uncertain and Opposite Effects from Shallow and Deep Clouds, in: Climate
924 Science for Serving Society: Research, Modeling and Prediction Priorities, edited by: Asrar, G.
925 R. and Hurrell, J. W., Springer Netherlands, Dordrecht, 105–149, https://doi.org/10.1007/978-
926 94-007-6692-1_5, 2013.
927 Rosenfeld, D., Andreae, M. O., Asmi, A., Chin, M., Leeuw, G., Donovan, D. P., Kahn, R.,
928 Kinne, S., Kivekäs, N., Kulmala, M., Lau, W., Schmidt, K. S., Suni, T., Wagner, T., Wild, M.,
929 and Quaas, J.: Global observations of aerosol-cloud-precipitation- climate interactions, 52, 750–
930 808, https://doi.org/10.1002/2013RG000441.Received, 2014.

931   Rosenfeld, D., Zheng, Y., Hashimshoni, E., Pöhlker, M. L., Jefferson, A., Pöhlker, C., Yu, X.,
932   Zhu, Y., Liu, G., Yue, Z., Fischman, B., Li, Z., Giguzin, D., Goren, T., Artaxo, P., Barbosa, H.
933   M. J., Pöschl, U., and Andreae, M. O.: Satellite retrieval of cloud condensation nuclei
934   concentrations by using clouds as CCN chambers, Proc Natl Acad Sci U S A,
935   https://doi.org/10.1073/pnas.1514044113, 2016.
936   Satheesh, S. K. and Ramanathan, V.: Large differences in tropical aerosol forcing at the top of
937   the atmosphere and Earth's surface, Nature, https://doi.org/10.1038/35011039, 2000.
938   Sciare, J., Oikonomou, K., Favez, O., Liakakou, E., Markaki, Z., Cachier, H., and Mihalopoulos,
939   N.: Long-term measurements of carbonaceous aerosols in the Eastern Mediterranean: evidence
940   of long-range transport of biomass burning, 8, 5551–5563, 2008.
941   Seinfeld, J. H., Bretherton, C., Carslaw, K. S., Coe, H., DeMott, P. J., Dunlea, E. J., Feingold, G.,
942   Ghan, S., Guenther, A. B., Kahn, R., Kraucunas, I., Kreidenweis, S. M., Molina, M. J., Nenes,
943   A., Penner, J. E., Prather, K. A., Ramanathan, V., Ramaswamy, V., Rasch, P. J., Ravishankara,
944   A. R., Rosenfeld, D., Stephens, G., and Wood, R.: Improving our fundamental understanding of
945   the role of aerosol–cloud interactions in the climate system, 113, 5781–5790,
946   https://doi.org/10.1073/pnas.1514043113, 2016.
947   Sharma, A. R. and Déry, S. J.: Variability and trends of landfalling atmospheric rivers along the
948   Pacific Coast of northwestern North America, https://doi.org/10.1002/joc.6227, 2020.
949   Sitnov, S. A., Mokhov, I. I., and Likhosherstova, A. A.: Exploring large-scale black-carbon air
950   pollution over Northern Eurasia in summer 2016 using MERRA-2 reanalysis data,
951   https://doi.org/10.1016/j.atmosres.2019.104763, 2020.
952   Sofiev, M., Soares, J., Prank, M., De Leeuw, G., and Kukkonen, J.: A regional-to-global model
953   of emission and transport of sea salt particles in the atmosphere,
954   https://doi.org/10.1029/2010JD014713, 2011.
955   Song, C. H. and Carmichael, G. R.: The aging process of naturally emitted aerosol (sea-salt and
956   mineral aerosol) during long range transport, 33, 2203–2218,
957   https://doi.org/https://doi.org/10.1016/S1352-2310(98)00301-X, 1999.
958   Stevens, B. and Feingold, G.: Untangling aerosol effects on clouds and precipitation in a
959   buffered system, https://doi.org/10.1038/nature08281, 2009.
960   Swap, R., Garstang, M., Macko, S. A., Tyson, P. D., Maenhaut, W., Artaxo, P., Kållberg, P., and
961   Talbot, R.: The long-range transport of southern African aerosols to the tropical South Atlantic,
962   101, 23777–23791, 1996.
963   Takemura, T., Uno, I., Nakajima, T., Higurashi, A., and Sano, I.: Modeling study of long-range
964   transport of Asian dust and anthropogenic aerosols from East Asia, 29, 11, 2002.
965   Takemura, T., Nozawa, T., Emori, S., Nakajima, T. Y., and Nakajima, T.: Simulation of climate
966   response to aerosol direct and indirect effects with aerosol transport-radiation model,
967   https://doi.org/10.1029/2004JD005029, 2005.
968   Tomasi, C., Vitale, V., Lupi, A., di Carmine, C., Campanelli, M., Herber, A., Treffeisen, R.,
969   Stone, R. S., Andrews, E., and Sharma, S.: Aerosols in polar regions: A historical overview
970   based on optical depth and in situ observations, 112, 2007a.
971   Tomasi, C., Vitale, V., Lupi, A., di Carmine, C., Campanelli, M., Herber, A., Treffeisen, R.,
972   Stone, R. S., Andrews, E., and Sharma, S.: Aerosols in polar regions: A historical overview
973   based on optical depth and in situ observations, 112, 2007b.
974   Wang, J. and Christopher, S. A.: Intercomparison between satellite-derived aerosol optical
975   thickness and PM2.5 mass: Implications for air quality studies,
976   https://doi.org/10.1029/2003GL018174, 2003.

977 Wang, S.-H., Tsay, S.-C., Lin, N.-H., Hsu, N. C., Bell, S. W., Li, C., Ji, Q., Jeong, M.-J.,
978 Hansell, R. A., and Welton, E. J.: First detailed observations of long-range transported dust over
979 the northern South China Sea, 45, 4804–4808, 2011a.
980 Wang, S.-H., Tsay, S.-C., Lin, N.-H., Hsu, N. C., Bell, S. W., Li, C., Ji, Q., Jeong, M.-J.,
981 Hansell, R. A., and Welton, E. J.: First detailed observations of long-range transported dust over
982 the northern South China Sea, 45, 4804–4808, 2011b.
983 Wang, Y., Zhang, Q. Q., He, K., Zhang, Q., and Chai, L.: Sulfate-nitrate-ammonium aerosols
984 over China: Response to 2000-2015 emission changes of sulfur dioxide, nitrogen oxides, and
985 ammonia, https://doi.org/10.5194/acp-13-2635-2013, 2013.
986 Wang, Y., Zheng, X., Dong, X., Xi, B., Wu, P., Logan, T., and Yung, Y. L.: Impacts of long-
987 range transport of aerosols on marine-boundary-layer clouds in the eastern North Atlantic, 20,
988 14741–14755, 2020a.
989 Wang, Z., Walsh, J., Szymborski, S., and Peng, M.: Rapid arctic sea ice loss on the synoptic time
990 scale and related atmospheric circulation anomalies, https://doi.org/10.1175/JCLI-D-19-0528.1,
991 2020b.
992 Weinzierl, B., Ansmann, A., Prospero, J. M., Althausen, D., Benker, N., Chouza, F., Dollner, M.,
993 Farrell, D., Fomba, W. K., Freudenthaler, V., Gasteiger, J., Groß, S., Haarig, M., Heinold, B.,
994 Kandler, K., Kristensen, T. B., Mayol-Bracero, O. L., Müller, T., Reitebuch, O., Sauer, D.,
995 Schäfler, A., Schepanski, K., Spanu, A., Tegen, I., Toledano, C., and Walser, A.: The Saharan
996 Aerosol Long-Range Transport and Aerosol–Cloud-Interaction Experiment: Overview and
997 Selected Highlights, Bull Am Meteorol Soc, 98, 1427–1451, https://doi.org/10.1175/BAMS-D-
998 15-00142.1, 2017.
999 Wu, M. L. C., Reale, O., Schubert, S. D., Suarez, M. J., Koster, R. D., and Pegion, P. J.: African
1000 easterly jet: Structure and maintenance, https://doi.org/10.1175/2009JCLI2584.1, 2009.
1001 Xi, X. and Sokolik, I. N.: Impact of Asian Dust Aerosol and Surface Albedo on
1002 Photosynthetically Active Radiation and Surface Radiative Balance in Dryland Ecosystems,
1003 2012, 276207, https://doi.org/10.1155/2012/276207, 2012.
1004 Xu, X., Wu, H., Yang, X., and Xie, L.: Distribution and transport characteristics of dust aerosol
1005 over Tibetan Plateau and Taklimakan Desert in China using MERRA-2 and CALIPSO data,
1006 https://doi.org/10.1016/j.atmosenv.2020.117670, 2020.
1007 Zhou, Y. and Kim, H.: Impact of Distinct Origin Locations on the Life Cycles of Landfalling
1008 Atmospheric Rivers Over the U.S. West Coast, https://doi.org/10.1029/2019JD031218, 2019.
1009 Zhu, Y. and Newell, R. E.: Atmospheric rivers and bombs, https://doi.org/10.1029/94GL01710,
1010 1994.
1011 Zhu, Y. and Newell, R. E.: A proposed algorithm for moisture fluxes from atmospheric rivers,
1012 https://doi.org/10.1175/1520-0493(1998)126<0725:APAFMF>2.0.CO;2, 1998.
1013